RESEARCH ARTICLE

Zongertinib (BI 1810631), an Irreversible HER2 TKI, Spares EGFR Signaling and Improves Therapeutic Response in Preclinical Models and Patients with HER2-Driven Cancers

Birgit Wilding[1], Lydia Woelflingseder[1], Anke Baum[1], Krzysztof Chylinski[1], Gintautas Vainorius[1], Neil Gibson[2], Irene C. Waizenegger[1], Daniel Gerlach[1], Martin Augsten[1], Fiona Spreitzer[1], Yukina Shirai[3], Masachika Ikegami[3], Sylvia Tilandyová[1], Dirk Scharn[1], Mark A. Pearson[1], Johannes Popow[1], Anna C. Obenauf[4], Noboru Yamamoto[5], Shunsuke Kondo[5], Frans L. Opdam[6], Annemarie Bruining[7], Shinji Kohsaka[3], Norbert Kraut[1], John V. Heymach[8], Flavio Solca[1], and Ralph A. Neumüller[1]

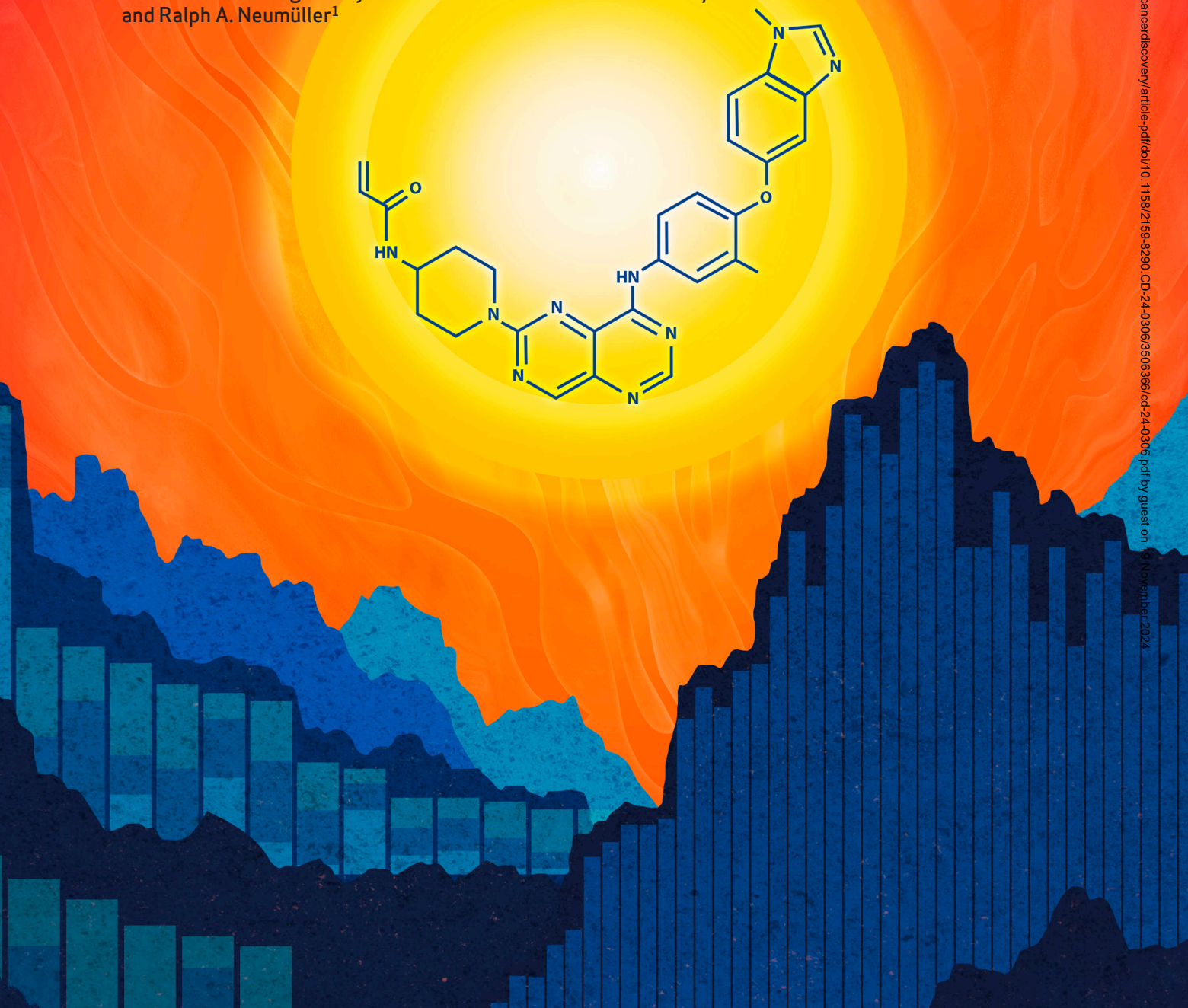

ABSTRACT Mutations in *ERBB2* (encoding HER2) occur in 2% to 4% of non–small cell lung cancer (NSCLC) and confer poor prognosis. ERBB-targeting tyrosine kinase inhibitors, approved for treating other HER2-dependent cancers, are ineffective in HER2-mutant NSCLC due to dose-limiting toxicities or suboptimal potency. We report the discovery of zongertinib (BI 1810631), a covalent HER2 inhibitor. Zongertinib potently and selectively blocks HER2, while sparing EGFR, and inhibits the growth of cells dependent on HER2 oncogenic driver events, including HER2-dependent human cancer cells resistant to trastuzumab deruxtecan. Zongertinib displays potent antitumor activity in HER2-dependent human NSCLC xenograft models and enhances the activities of antibody–drug conjugates and $KRAS^{G12C}$ inhibitors without causing obvious toxicities. The preclinical efficacy of zongertinib translates in objective responses in patients with HER2-dependent tumors, including cholangiocarcinoma (SDC4–NRG1 fusion) and breast cancer (V777L HER2 mutation), thus supporting the ongoing clinical development of zongertinib.

SIGNIFICANCE: HER2-mutant NSCLC poses a challenge in the clinic due to limited options for targeted therapies. Pan-ERBB blockers are limited by wild-type EGFR–mediated toxicity. Zongertinib is a highly potent and wild-type EGFR–sparing HER2 inhibitor that is active in HER2-driven tumors in the preclinical and clinical settings.

INTRODUCTION

The ERBB family receptor tyrosine kinases (RTK) are important for normal development and physiology (1–3). In humans, the ERBB family includes the following members: EGFR, also referred to as HER1 (encoded by *EGFR*), HER2 (encoded by *ERBB2*), HER3 (encoded by *ERBB3*), and HER4 (encoded by *ERBB4*). These receptors form homodimers and heterodimers upon ligand activation. HER2 lacks a known ligand but is the preferred dimerization partner of other family members. The MAPK and PI3K/AKT pathways constitute the two major signaling pathways downstream of ERBB family receptors (2).

Aberrant activation of ERBB family members through various mechanisms plays a crucial role in the development and progression of a variety of cancer types (2). Overexpression of HER2, due to *ERBB2* amplification, occurs in ~20% of human breast cancers and is associated with an aggressive phenotype and a historically poor prognosis (4). Monoclonal antibodies, including trastuzumab and pertuzumab, display clinical benefit in patients with HER2-positive breast cancer (5, 6). More recently, trastuzumab emtansine (T-DM1; 7) and trastuzumab deruxtecan (T-DXd; 8), two antibody–drug conjugates (ADC), have demonstrated clinical efficacy, leading to their approval for patients with HER2-positive breast cancer resistant to trastuzumab (9). T-DXd is also approved for patients with HER2-low metastatic breast cancer, HER2-positive stomach cancer, and HER2-mutated lung cancer who have received prior systemic therapy. More recently, T-DXd received accelerated approval from the FDA for treatment of patients with unresectable or metastatic HER2-positive ($IHC3^+$) solid tumors who received prior treatment and have no satisfactory alternative treatment option.

In addition to overexpression, ERBB family members can be aberrantly activated by oncogenic mutations (10, 11). Mutational activation of HER2 occurs in many types of solid tumors, including non–small cell lung cancer (NSCLC). These mutations increase the kinase activity by either favoring an active conformation or inducing homodimerization or heterodimerization of members of the ERBB family of RTKs (11). HER2 mutations occur within 2% to 4% of NSCLC and have emerged as important oncogenic drivers (10, 12–16). The most commonly found mutation in NSCLC is a 12 base pair (bp) insertion in *ERBB2* exon 20 that results in the duplication of amino acids YVMA in HER2 ($HER2^{YVMA}$; ref. 15). HER2 mutations are associated with aggressive disease progression and poor clinical outcomes (10, 17) in response to chemotherapy and immunotherapy (18). Several pan-ERBB inhibitors, including afatinib

[1]Boehringer Ingelheim RCV GmbH & Co KG, Vienna, Austria. [2]Translational Medicine and Clinical Pharmacology, Boehringer Ingelheim Pharma GmbH & Co. KG, Biberach, Germany. [3]Division of Cellular Signaling, National Cancer Center Research Institute, Tokyo, Japan. [4]Research Institute of Molecular Pathology (IMP), Vienna BioCenter (VBC), Vienna, Austria. [5]Department of Experimental Therapeutics, National Cancer Center Hospital, Tokyo, Japan. [6]Division of Medical Oncology, Department of Clinical Pharmacology, Antoni van Leeuwenhoek/The Netherlands Cancer Institute, Amsterdam, the Netherlands. [7]Department of Radiology, Antoni van Leeuwenhoek/The Netherlands Cancer Institute, Amsterdam, the Netherlands. [8]Department of Thoracic/Head and Neck Medical Oncology, The University of Texas MD Anderson Cancer Center, Houston, Texas.

Corresponding Authors: Birgit Wilding, Boehringer Ingelheim RCV GmbH & Co KG, Dr.-Boehringer-Gasse 5-11, Vienna 1121, Austria. E-mail: birgit.wilding@boehringer-ingelheim.com; and Ralph A. Neumüller, Boehringer Ingelheim RCV GmbH & Co KG, Dr.-Boehringer-Gasse 5-11, Vienna 1121, Austria. E-mail: ralph.neumueller@boehringer-ingelheim.com

Cancer Discov 2024;XX:1–20

doi: 10.1158/2159-8290.CD-24-0306

(19–21), poziotinib (22–26), neratinib (27), and pyrotinib (28), have been investigated in patients with HER2-mutant NSCLC but have shown limited efficacy in clinical studies. Pan-ERBB inhibitors block all ERBB family members, share common on-target and potentially dose-limiting adverse effects, including skin rashes (29) and diarrhea, due to inhibiting wild-type (WT) EGFR and thus are hampered in developing their full potential clinical activity in HER2 exon 20–dependent tumors (30). ADCs have demonstrated clinical activity in HER2 mutation–driven tumors. T-DM1 was shown to be an active agent in a subset of patients with HER2-mutant lung cancer (31). T-DXd displayed activity in patients with HER2-mutant NSCLC (32, 33). The results from the DESTINY-Lung01 and -Lung02 trials resulted in the FDA approval of T-DXd, representing a new standard-of-care treatment for patients with previously treated HER2-mutant NSCLC. However, treatment of patients with NSCLC with T-DXd is also associated with treatment-related adverse events (AE), including interstitial lung disease or pneumonitis (34). Therefore, there exists a critical unmet medical need for selective, orally available, and well-tolerated HER2 tyrosine kinase inhibitors (TKI) that effectively target HER2 mutants while preserving $EGFR^{WT}$ activity.

ERBB signaling can also be aberrantly activated through alterations in their ligands. In addition to increased expression, fusions of the neuregulin-1 (*NRG1*) gene, although very rare, have been clinically documented (35). These fusions retain the EGF-like domain in the extracellular portion and are competent to engage with HER3 and HER4, triggering oncogenic signaling through HER2-, HER3-, or HER4-containing heterodimers (35, 36).

ERBB signaling activates the MAPK and PI3K pathways. Hyperactivation of these pathways drives neoplastic transformation and tumor maintenance. The MAPK signal transducer KRAS is frequently mutated in various types of carcinomas (37, 38). In NSCLC, the substitution of glycine 12 with cysteine (G12C) is a common KRAS mutation, occurring in ~13% of cases (38). Downstream KRAS mutations represent a resistance mechanism to EGFR inhibition (39). On the other hand, adaptive activation of RTKs, including EGFR and HER2, has been shown to confer resistance to KRAS inhibition in preclinical studies (39, 40). Coinhibition of EGFR has been shown to potentiate the effect of $KRAS^{G12C}$ inhibitors, including sotorasib and adagrasib, that are approved for the treatment of human NSCLC with $KRAS^{G12C}$ mutations. The reported overall response rate (ORR) for $KRAS^{G12C}$ varies between 28% and 53% (40–43) depending on the compound, dosing schedule, and clinical phase, but resistance invariably occurs (40, 44–48).

To address the limitations of conventional pan-ERBB inhibitors and improve therapeutic outcomes for patients with HER2-driven tumors, we have identified and optimized TKIs that effectively inhibit WT HER2 and HER2 oncogenic variants with high selectivity over $EGFR^{WT}$. We recently reported the discovery of two probe compounds, BI-4142 and BI-1622, which possessed the desired potency and selectivity, but were not suited for clinical development (49). Here, we report the discovery and characterization of zongertinib (BI 1810631), a clinical candidate optimized for use in patients with the promise of fulfilling the unmet medical need of a specific and well-tolerated therapy tailored to HER2-mutant NSCLC and other HER2-dependent malignancies. Zongertinib is a potent covalent HER2 inhibitor that spares $EGFR^{WT}$ and is both efficacious and tolerated as monotherapy or in combination with HER2-targeting ADCs or $KRAS^{G12C}$ inhibitors in preclinical studies. Additionally, we describe the preliminary single-agent clinical activity of zongertinib in patients with HER2 mutations. As such, zongertinib represents a promising treatment option for patients with HER2-dependent cancers.

RESULTS

We set out to develop an $EGFR^{WT}$-sparing HER2 inhibitor clinical candidate with improved properties over previously described TKIs (a manuscript describing the multiparameter optimization for a clinical candidate with improved properties compared with BI-4142 and BI-1622 is in preparation; 49). This led to the discovery of zongertinib (Fig. 1A–C; Supplementary Figs. S1A, S1B, S2A, and S2B), which displayed high potency against $HER2^{YVMA}$ and selectivity against $EGFR^{WT}$ in a phosphorylation assay in HEK cells (Fig. 1A). These findings were recapitulated in proliferation assays using Ba/F3 cells engineered to be dependent on $EGFR^{WT}$ or $HER2^{YVMA}$, in which the compound displayed ~100-fold $EGFR^{WT}$-sparing activity. Zongertinib is a covalent inhibitor that forms a covalent bond between its acrylamide moiety and cysteine 805 of HER2. We confirmed the relevance of covalent binding in the activity of zongertinib using an engineered Ba/F3 cell line dependent on $HER2^{YVMA,C805S}$, in which cysteine 805 is replaced by serine and, therefore, can no longer form a covalent bond with zongertinib. The antiproliferative IC_{50} value of zongertinib was increased from 16 nmol/L in the $HER2^{YVMA}$ Ba/F3 cell line to 554 nmol/L in the $HER2^{YVMA,C805S}$ Ba/F3 cell line. The importance of the covalent binding in the activity of zongertinib was further substantiated by the reduced potency observed with BI-3999, an acetamide-matched pair compound of zongertinib that is unable to form a covalent bond with HER2, in which equivalent potency in Ba/F3 $HER2^{YVMA}$ cells was observed to that measured for zongertinib in the $HER2^{YVMA,C805S}$ cell line. Additionally, zongertinib shows an antiproliferative effect in other $HER2^{YVMA}$- as well as $HER2^{WT}$-dependent human cancer cell lines, whereas it maintains a high selectivity in an $EGFR^{WT}$-dependent human cancer cell line (Fig. 1A). Note: As human cancer cell lines carrying the $HER2^{YVMA}$ variant are not available, we utilized mechanistic models engineered to be dependent on $HER2^{YVMA}$ (PC-9: oncogene swap by viral expression of $HER2^{YVMA}$ and subsequent *EGFR* knockout (KO); PC-9 cells carry the $EGFR^{del19}$ variant; NCI-H2170: $HER2^{YVMA}$ knock-in; 49).

We collected a set of non-GMP CMC (chemistry, manufacturing and controls) and pharmacokinetic (PK) data to evaluate zongertinib further. Zongertinib exhibited kinetic solubility of <0.001 mg/mL at pH levels 4.5 and 6.8, which translated into comparable solubility (<0.001 mg/mL) also in fasted state–simulated intestinal fluid and somewhat improved solubility (0.03 mg/mL) in fed state–simulated intestinal fluid (Fig. 1B). The permeability of zongertinib in Madin-Darby canine kidney cells (MDCK) assays was good, with specific BCRP (breast cancer resistance protein)-mediated efflux observed (efflux ratio MDCK BCRP = 18). Zongertinib was highly bound to plasma protein across species and showed low clearance across species in an *in vitro* hepatocyte stability assay (Fig. 1B). Although the low clearance suggested a promising

A

		BI 1810631		BI-3999	
Pathway modulation pIC_{50} ± SEM (IC_{50}, *n*)	pHER2 HEK $HER2^{YVMA}$	7.92 ± 0.04	(12 nmol/L, *n* = 11)	7.91 ± 0.08	(12 nmol/L, *n* = 2)
	pEGFR HEK $EGFR^{WT}$	6.24 ± 0.05	(576 nmol/L, *n* = 10)	<5	(>10,000 nmol/L, *n* = 2)
Antiproliferative effect on Ba/F3 cells pIC_{50} ± SEM (IC_{50}, *n*)	Ba/F3 $HER2^{YVMA}$	7.79 ± 0.05	(16 nmol/L, *n* = 29)	6.31 ± 0.10	(483 nmol/L, *n* = 8)
	Ba/F3 $HER2^{YVMA, C805S}$	6.26 ± 0.02	(554 nmol/L, *n* = 26)	6.28 ± 0.11	(518 nmol/L, *n* = 4)
	Ba/F3 $EGFR^{WT}$	5.81 ± 0.05	(1,540 nmol/L, *n* = 8)	<5.3	(>5,000 nmol/L, *n* = 7)
Potency, antiproliferative effect on cancer cells pIC_{50} ± SEM (IC_{50}, *n*)	NCI-H2170 $HER2^{WT}$	8.20 ± 0.05	(6.3 nmol/L, *n* = 9)	6.41 ± 0.21	(386 nmol/L, *n* = 2)
	NCI-N87 $HER2^{WT}$	8.78 ± 0.07	(1.7 nmol/L, *n* = 7)	n/d	
	NCI-H2170 $HER2^{YVMA}$	7.71 ± 0.03	(20 nmol/L, *n* = 22)	5.88 ± 0.24	(1,290 nmol/L, *n* = 3)
	PC-9 $HER2^{YVMA}$	7.73 ± 0.03	(19 nmol/L, *n* = 29)	<5.5	(>3,000 nmol/L, *n* = 2)
	A431 $EGFR^{WT}$	<5.3	(>5,000 nmol/L, *n* = 8)	<5.3	(>5,000 nmol/L, *n* = 2)

B

		BI 1810631			
Physicochemical properties	Molecular weight	535.61 g/mol			
	tPSA | logP	123 Å² | 4.6			
	Solubility at pH 4.5 and 6.8	<0.001 mg/mL			
	Solubility FaSSIF	<0.001 mg/mL			
	Solubility FeSSIF	0.03 mg/mL			
***In vitro* DMPK**	MDCK PgP	$P_{app, AB}$ = 20 × 10^{-6} cm/seconds, efflux ratio = 1.1			
	MDCK BCRP	$P_{app, AB}$ = 4.8 × 10^{-6} cm/seconds, efflux ratio = 18			
	PPB f_u (%) m | r | d | h	0.2	0.3	0.7	0.2
	Hepatocytes CL_{int} (µL/minute/10^6 cells) m | r | d | h	8.0	3.5	2.2	3.5

C

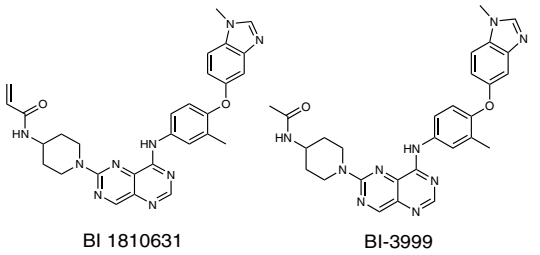

D

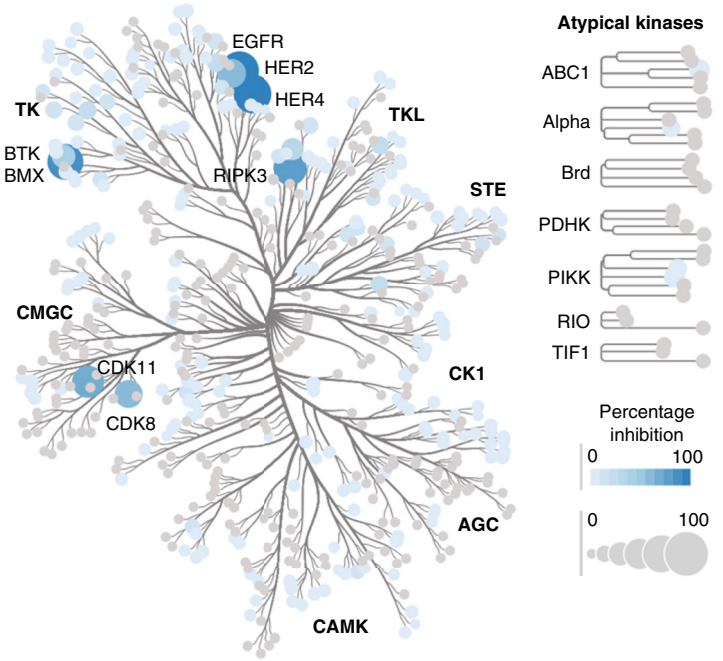

E

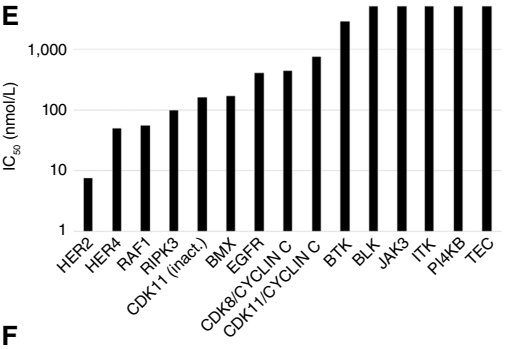

F

Summary of the prediction of BI 1810631 pharmacokinetics and therapeutic dose in humans		
Clearance	1.5 mL × $minute^{-1}$ × kg^{-1}	*In vitro-in vivo* correlation**
V_{ss}	0.3 l × kg^{-1}	Mean over animal species***
F	41%	Mean over animal species
k_a	0.93 $hour^{-1}$	Mean over animal species
t_{max}	1.8 hour	Bateman function****
Exposure target based on a quantitative PC-9 $HER2^{YVMA}$ PK/TGI model		
$AUC_{SS, tau\ 24\ hours}$	9,700 nmol/L × h	Bateman function****
$c_{max, ss}$	875 nmol/L | 1,700 nmol/L*	Bateman function****
$c_{min, ss}$	62 nmol/L | 3 nmol/L*	Bateman function****
Therapeutic dose	40 mg twice daily	

** values for twice daily \| every day scheduling ** using hepatocyte metabolic stability data ***corrected for PPB ****derived from a multiple dose simulation of the human PK at 40 mg twice daily*

Figure 1. Zongertinib is a highly selective covalent HER2 inhibitor. **A,** Potency of zongertinib and the noncovalent matched pair binder BI-3999 in a cellular phosphorylation assay using HEK cells and antiproliferative assays using Ba/F3 and human cancer cell lines. **B,** Physicochemical parameters and *in vitro* DMPK of zongertinib. CL_{int}, intrinsic clearance; d, dog; f_u, fraction unbound; FaSSIF, fasted state–simulated intestinal fluid; FeSSIF, fed state–simulated intestinal fluid; h, human; m, mouse; PPB, plasma–protein binding; r, rat. PPB data were obtained using the methods reported in the Methods section. **C,** Chemical structures of zongertinib and the noncovalent matched pair binder BI-3999. **D,** Kinase selectivity profile of zongertinib: Phylogenetic tree for protein kinases with the size and color of nodes indicating inhibition at 1 µmol/L in *in vitro* kinase assays. The kinase assays reported in the figure were performed as single measurements. **E,** IC_{50} values of zongertinib in a set of selected kinases in a biochemical kinase assay, *n* = 1. **F,** Summary of the prediction of zongertinib PK and therapeutic dose in human. $AUC_{ss, tau\ 24\ hours}$, AUC at steady state at a dosing interval of 24 hours; DMPK, x; F, oral bioavailability; k_a, absorption rate constant; ; t_{max}, time of maximum plasma concentration; V_{ss}, volume of distribution at steady state.

in vivo PK profile, zongertinib also showed low solubility and high permeability, which might result in dissolution rate–limited absorption. We therefore investigated *in vivo* mouse PK after oral administration of 3 and 100 mg/kg to confirm dose linearity in this dosing range. The mouse PK studies after i.v. and oral dosing showed dose linearity in the tested dose range, low *in vivo* clearance, and good oral bioavailability. With the *in vitro* and *in vivo* clearance correlation confirmed in the mouse model, we investigated the *in vivo* PK additionally in rat, dog, and minipig models and confirmed a good *in vitro* and *in vivo* correlation and moderate to good oral bioavailability across species (Supplementary Fig. S1B).

Zongertinib showed high selectivity against a broad panel of kinases. It achieved >80% inhibition of only two [HER4 and BMX (in addition to HER2)] out of 397 kinases in a single-point (at 1 μmol/L) inhibition assay (Fig. 1D). Kinases that were inhibited with >50% at 1 μmol/L as well as kinases with a cysteine homologous to C805 of HER2 were additionally tested in full dose–response curves (Fig. 1E). The results confirmed that zongertinib had high potency for HER2 while showing excellent selectivity over other kinases, with greater than 25-fold selectivity (IC_{50}) over EGFR (Fig. 1E).

A comprehensive PK profiling of zongertinib *in vitro* and *in vivo*, using mouse, rat, dog, and minipig models (data available in Supplementary Fig. S1B), enabled prediction of human PK parameters (Fig. 1F). By conducting a regression analysis of the predicted *in vitro* clearance obtained from hepatocyte incubation and the corresponding *in vivo* plasma clearance, a low plasma clearance of 1.5 mL × minutes^{-1} × kg^{-1} for zongertinib in humans was predicted. Moreover, zongertinib was predicted to exhibit a low volume of distribution (V_{ss}) of 0.3 L × kg^{-1}, an absorption rate constant of 0.9 hour^{-1}, and an oral bioavailability of 41%. The PK plasma profile of zongertinib was simulated using the predicted human PK parameters.

As human cancer cell lines carrying the HER2^{YVMA} variant are not available, we utilized the abovementioned mechanistic models engineered to be dependent on HER2^{YVMA} (49) for predicting the human dose. These predicted human efficacious exposures were incorporated into a PK/tumor growth inhibition (TGI) model using PC-9 HER2^{YVMA} tumor growth kinetics obtained from prior *in vivo* xenograft experiments (49). The exposure of a human dose of 40 mg twice a day was estimated to be sufficient to achieve TGI >100% in patients.

We compared the selective activity on HER2^{YVMA} over EGFR^{WT} of zongertinib in Ba/F3 survival inhibition assay with those of >70 TKIs, including EGFR inhibitors and pan-ERBB inhibitors, in preclinical development or approved for clinical use [see (49) for the full list]. We quantified the difference between the potency on HER2^{YVMA} and that on EGFR^{WT} of these inhibitors using a selectivity index [see (49) for details]. Zongertinib showed a high selectivity (Fig. 2A), further underlining the EGFR^{WT}-sparing activity.

The selectivity of zongertinib was compared with the pan-ERBB blocker poziotinib in Ba/F3 cell models engineered to be dependent on HER2^{YVMA}, EGFR^{WT}, or an EGFR oncogenic mutant (EGFR^{del19} or EGFR^{del19,T790M}). Consistent with the screen result, zongertinib displayed better selectivity than poziotinib in inhibiting HER2^{YVMA} over EGFR^{WT} and EGFR^{del19} (Fig. 2B). The potency of zongertinib against a panel of HER2-mutant variants found in patients with cancer was then assessed. Using Ba/F3 cell models engineered to be dependent on EGFR^{WT}, HER2^{WT}, and various HER2 variants, we found that zongertinib had a strong antiproliferative activity (in the single-digit or low double-digit nanomolar range) against HER2^{WT} and all tested HER2 variants while maintaining a selectivity window versus EGFR^{WT} (Fig. 2C). This analysis was extended to a wider array of HER2 variants spanning the extracellular, transmembrane, and tyrosine kinase domains and other mutations (Supplementary Fig. S3A; Supplementary Table S1) using a previously published protocol (50). We found that zongertinib possesses strong antiproliferative activity against all tested variants but did not inhibit cells dependent on EGFR^{L858R,T790M}, EGFR^{L858R,T790M,C797S}, and KRAS^{G12D}, which were used as controls.

These studies were further extended to assess the potency of zongertinib to inhibit the proliferation of a panel of human cancer cell lines with different dependencies on EGFR or HER2 (Fig. 2D). We found that zongertinib displayed high potency (IC_{50} <100 nmol/L) against all cell lines dependent on HER2, including engineered lines expressing HER2^{YVMA} (NCI-H2170 HER2^{YVMA} IC_{50} = 20 nmol/L; PC-9 EGFR^{KO},HER2^{YVMA} IC_{50} = 19 nmol/L), cell lines harboring an NRG1 gene fusion [MDA-MB-175-VII with a DOC4 (TENM4)-NRG1 fusion], or cell lines expressing high levels of HER2^{WT} (AU565, BT-474, HCC1419, HCC1954, NCI-H2170, and OE19). Zongertinib was not active in A431, HCC4006, and HT115 cell lines, for which HER2 is not an oncogenic driver. Of note, the A431 cell line is dependent on EGFR^{WT} (A431 EGFR^{WT} IC_{50} >5,000 nmol/L). These studies in cancer-derived cell lines confirmed the selectivity and potency of zongertinib for HER2 versus EGFR, including mutant variants and cell lines driven by high levels of HER2^{WT} (Fig. 2D).

The effect of zongertinib on HER2 phosphorylation and downstream pathway modulation was assessed in cancer cell lines (Fig. 2E and F; Supplementary Fig. S3B and S3C). We consistently noted a dose-dependent downregulation of HER2 downstream signaling nodes, including phosphorylated ERK and AKT, as well as the MAPK target gene and negative feedback regulator DUSP6, in HER2-dependent cells treated with zongertinib (Fig. 2E and F; additional cell lines in supplementary Fig. S3C). In a 48-hour time course experiment, zongertinib reduced pHER2 levels in NCI-N87 cells and triggered a downmodulation of MAPK and PI3K pathway signaling. In addition, zongertinib treatment induced a cell-cycle block (cyclin D1 downregulation) and cell death (cleaved PARP and caspase 3; Fig. 2E). Although zongertinib treatment reduced EGFR phosphorylation (presumably due to inhibiting HER2-mediated transphosphorylation of EGFR) in HER2-dependent cell lines expressing EGFR and high levels of HER2 (NCI-N87), it reduced phosphorylated EGFR in EGFR^{WT}-dependent cell lines (A431) only at high doses (>100 nmol/L; Fig. 2F). At the transcriptional level, zongertinib induced a time- and dose-dependent reduction of the MAPK pathway activation score (MPAS) (51) score, a measurement of the expression of a subset of MAP kinase pathway downstream genes (Fig. 2G–I; Supplementary Fig. S3D–S3F), thereby providing a measure of MAPK pathway activity, in a PC-9 cell line engineered to be dependent on HER2^{YVMA} (Fig. 2G). Validating the MPAS score result, zongertinib induced a dose-dependent reduction in the expression of ERK pathway targets, including

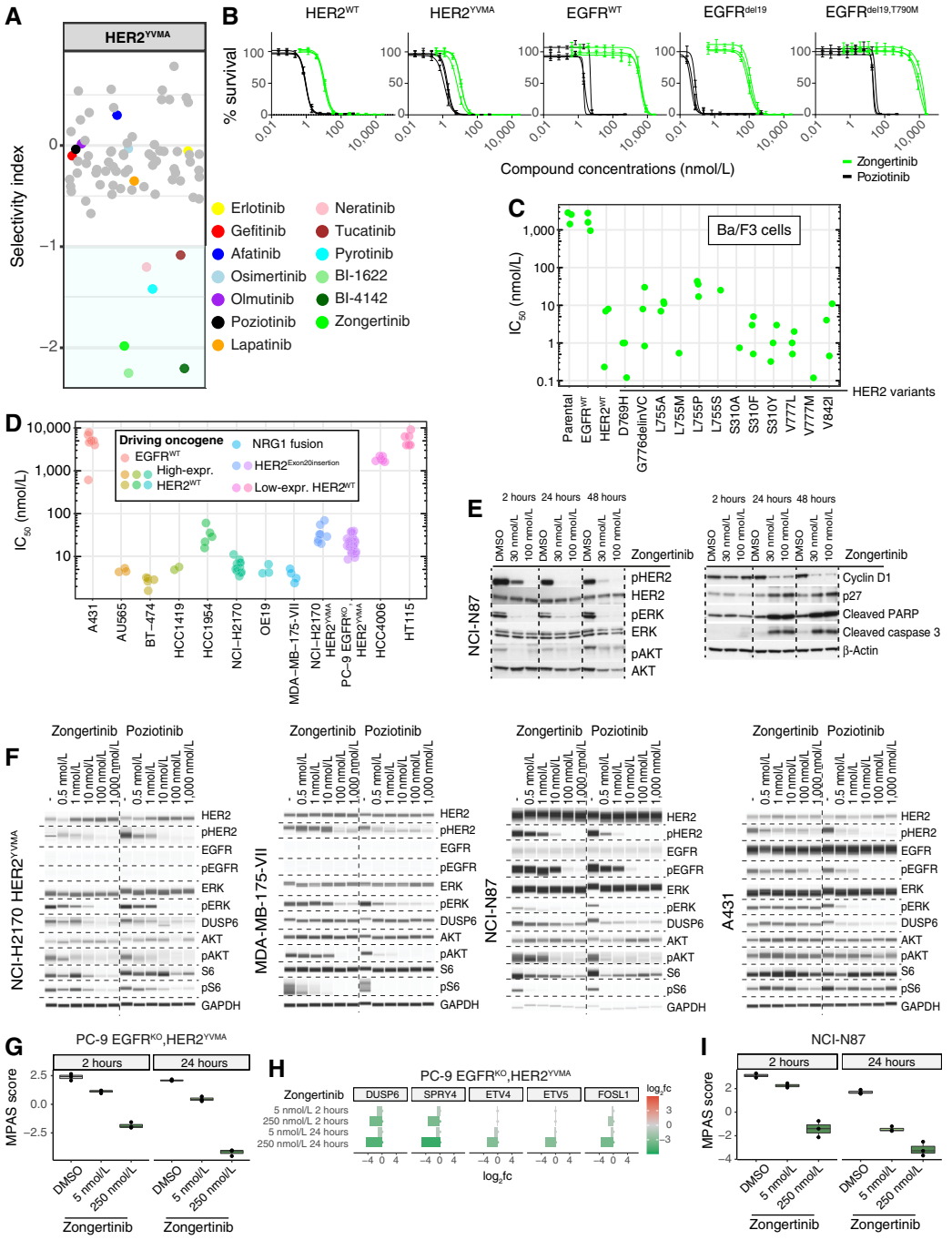

Figure 2. Zongertinib is active on HER2 mutation or overexpression–dependent cell lines and spares EGFR^{WT}. **A,** Selectivity index plot for proliferation assay in Ba/F3 cells dependent on HER2^{YVMA} in reference to EGFR^{WT}. Formula for the calculation of the selectivity index is provided in (49). The screen of TKIs was conducted in a single experiment without repetition except for zongertinib ($n = 3$). Each dot represents one (except zongertinib, where the dot represents the mean) indicated compound measurement. **B,** Dose–response curves of zongertinib and poziotinib in Ba/F3 cells dependent on HER2 and EGFR variants. **C,** IC_{50} values for zongertinib in Ba/F3 cells dependent on EGFR^{WT}, HER2^{WT}, or indicated HER2 variants. Each dot represents the result from an independent dose–response experiment using the indicated cell line. *Y*-axis: IC_{50} in nmol/L. **D,** Antiproliferative activity of zongertinib in a panel of cancer cells. *X*-axis: cell lines arranged according to oncogenic mechanism. *Y*-axis: IC_{50} in nmol/L. EGFR and HER2 status is indicated in the inset. Individual points indicate individual measurements in fully independent experiments. **E,** Modulation of HER2 signaling at the level of HER2 and downstream mediators in NCI-N87 cells upon zongertinib treatment at different doses and time points. Plots show total protein for HER2, ERK, AKT, cyclin D1, p27, cleaved caspase 3, and cleaved PARP as well as phosphorylated HER2 (Y1196), ERK, and AKT (S473). Actin used as the loading control is also shown. **F,** Modulation of HER2 and EGFR as well as their downstream mediators in H2170 HER2^{YVMA}, MDA-MB-175-VII, NCI-N87 (all HER2-driven), and A-431 (EGFR^{WT}-driven) cells upon zongertinib or poziotinib treatment. Plots show total protein for HER2, EGFR, ERK, AKT, S6, and DUSP6 as well as phosphorylated HER2, EGFR, ERK, S6, and AKT. GAPDH used as the loading control is also shown. **G,** Downregulation of MPAS genes (subset of MAP kinase pathway downstream genes) in PC-9 EGFR^{KO},HER2^{YVMA} cells upon zongertinib treatment *in vitro*. **H,** Modulation of MAPK downstream genes in PC-9 EGFR^{KO},HER2^{YVMA} cells upon zongertinib treatment. **I,** Downregulation of MPAS genes in NCI-N87 cells upon zongertinib treatment *in vitro*. NOS, x; TNBC, x.

DUSP6, *SPRY4*, *ETV4*, *ETV5*, and *FOSL1* (Fig. 2H). A similar time- and dose-dependent reduction of the MPAS score was observed in the human gastric cancer cell line NCI-N87, which is dependent on overexpressed HER2^{WT} (Fig. 2I). Collectively, these data suggest that zongertinib elicits its antiproliferative activity by blocking HER2-mediated signaling.

The antiproliferative activity of zongertinib and BI-1622, a structurally distinct HER2 inhibitor, was further evaluated against a large pool of barcoded human cancer cell lines [profiling relative inhibition simultaneously in mixtures (PRISM); Fig. 3A; Supplementary Figs. S4A–S4D, S5A and S5B; Supplementary Table S2; refs. 52, 53]. The expression level of HER2 was strongly correlated with sensitivity across these lines. Analysis of proteome and transcriptome data revealed that HER2 mRNA and protein levels are highly correlated across human cancer cell lines (Fig. 3B). Consistently, HER2 protein levels were highly correlated with sensitivity to zongertinib (Supplementary Fig. S5A). We selected a subset of cells for independent validation and confirmed the trend that HER2-overexpressing cell lines displayed preferential sensitivity to zongertinib (Fig. 3C). Consistently, subsequent Western blotting analyses confirmed high ERBB pathway activity in selected sensitive cell lines (Fig. 3D), with the antibody directed against phosphorylated tyrosine 1248 of HER2 showing the best separation between sensitive and insensitive cell lines.

Next, we evaluated gene expression results from more than 60,000 real-world tumor samples from Tempus AI across all major tumor indications for *ERBB2* gene amplification and HER2 overexpression. Besides confirming well-documented amplification frequencies of *ERBB2* in cancers, including breast and endometrial tumors (54, 55), this analysis identified HER2 overexpression in many other cancer types (Fig. 3E; Supplementary Table S3). In NSCLC, although only 1.7% of cases showed *ERBB2* amplification, 11.1% of cases with low-amplified and 8.7% of cases with diploid ERBB2 showed HER2 overexpression (Fig. 3E). These findings suggest that besides patients whose tumors have *ERBB2* gene amplification (copy number ≥6) additional patients might benefit from a HER2-selective TKI.

The activity of zongertinib *in vivo* was assessed using mouse xenograft models. We first tested NCI-N87 cells, which carry an *ERBB2* gene amplification. Zongertinib dose-dependently inhibited growth of tumors, delaying tumor growth at 2.5 mg/kg twice a day and 5 mg/kg every day and shrinking tumors at doses of 5 mg/kg twice a day and 10 mg/kg every day and above (Fig. 4A). Consistent with on-target activity, zongertinib suppressed HER2 phosphorylation and concurrently markers of downstream MAPK and PI3K signaling (Fig. 4B). Zongertinib also dose-dependently inhibited tumors formed from PC-9 EGFR^{KO},HER2^{YVMA} cells, dependent on HER2^{YVMA}, as validated by ARTi (Fig. 4C–E; ref. 56). It delayed tumor growth at 3 mg/kg twice a day and shrank tumors at 10 mg/kg twice a day (Fig. 4F). The ARTi system demonstrated that the engineered PC-9 model is HER2^{YVMA}-dependent, as a highly validated ARTi–short hairpin RNAmir (shRNAmir) reagent was used to knock down the HER2^{YVMA}-ARTi transgene (Fig. 4C; ref. 56). The loss of HER2^{YVMA} expression and downstream signaling markers were assessed after 48 hours of *in vitro* doxycycline treatment (Fig. 4E). Zongertinib, poziotinib, and the EGFR inhibitor erlotinib were assessed in mice bearing a NSCLC patient-derived xenograft (PDX) model that expressed HER2^{YVMA}, CTG-2543 (Fig. 4G). Erlotinib at 75 mg/kg resulted in modest TGI but no regressions. Poziotinib at the maximum tolerated dose (MTD) of 1 mg/kg every day effectively shrank tumors. Zongertinib at 30 mg/kg twice a day shrank tumors to a similar extent to poziotinib at 1 mg/kg, whereas zongertinib at 100 mg/kg induced deeper regressions while being well tolerated, as assessed by body weight change (Fig. 4G; Supplementary Fig. S6A). In order to link efficacy with biomarker modulation, we performed RNA sequencing (RNA-seq) in a PC-9 EGFR^{KO},HER2^{YVMA} xenograft model (Fig. 4H). The MPAS score (51) revealed moderate modulation for the 3 and 5 mg/kg zongertinib treatment groups and a more pronounced modulation for the 10 mg/kg groups. The effect of the MAPK pathway activity modulation was consistently stronger at the 6 hour versus the 2 hour time point, and recovery of the pathway activity was observed at the 24 hour time point (measured only for the 10 mg/kg groups). Notably, the MPAS signature modulation was comparable between the every day and twice a day dosing schedules (Fig. 4H). A prominent reduction of HER2 phosphorylation upon 10 or 20 mg/kg zongertinib after 2, 6, and 24 hours provided additional evidence for on-target activity in a PC-9 EGFR^{KO},HER2^{YVMA} xenograft model (Fig. 4I).

Zongertinib consistently inhibits downstream signaling of HER2 and the proliferation of cancer cells dependent on high expression of HER2^{WT} (Figs. 2–4). Antibody-based therapeutics are dependent on expression of the target in tumors but may still provide benefit, as shown by the recent accelerated approval of Enhertu, T-DXd, in HER2-low patients. Resistance to ADC therapeutics, such as T-DXd, can potentially occur through upregulation of intracellular pathways that decrease the activity of the payload in cancer cells that retain HER2 expression. We speculate that the differing mechanism of action of kinase inhibitors to antibody-based therapeutics could offer an opportunity to address resistance, which, to our knowledge, was not shown for an EGFR^{WT}-sparing HER2 inhibitor. We therefore investigated whether zongertinib was efficacious in human cancer cells dependent on high expression of HER2^{WT} but resistant to HER2-targeting ADCs. To generate T-DXd–resistant models, we used the NCI-N87 model and treated tumor-bearing mice with three cycles of T-DXd, harvested tumors that regrew, and then cultivated tumor cells *in vitro* (Fig. 5A). We treated parental and T-DXd–resistant NCI-N87 cells with deruxtecan (the T-DXd payload), T-DXd, and zongertinib (Fig. 5B and C). Inhibition of HER2 phosphorylation in both parental and T-DXd–resistant NCI-N87 cells was observed with zongertinib but not T-DXd (Fig. 5B). As expected, parental NCI-N87 cells were sensitive to both T-DXd and deruxtecan, whereas T-DXd–resistant cells were resistant to both T-DXd and deruxtecan, with at least a 100-fold difference in their IC_{50} values. Surprisingly, both parental and resistant NCI-N87 cells were sensitive to zongertinib, with less than a 10-fold difference in their IC_{50} values (Fig. 5C).

Pan-ERBB inhibitors were shown to induce increased ADC internalization through receptor ubiquitination (57), a mechanism that could be driven by individual ERBB members or a combination. It is, however, not clear whether a covalent HER2-selective, EGFR^{WT}-sparing compound would serve as a good combination partner for HER2-directed ADCs.

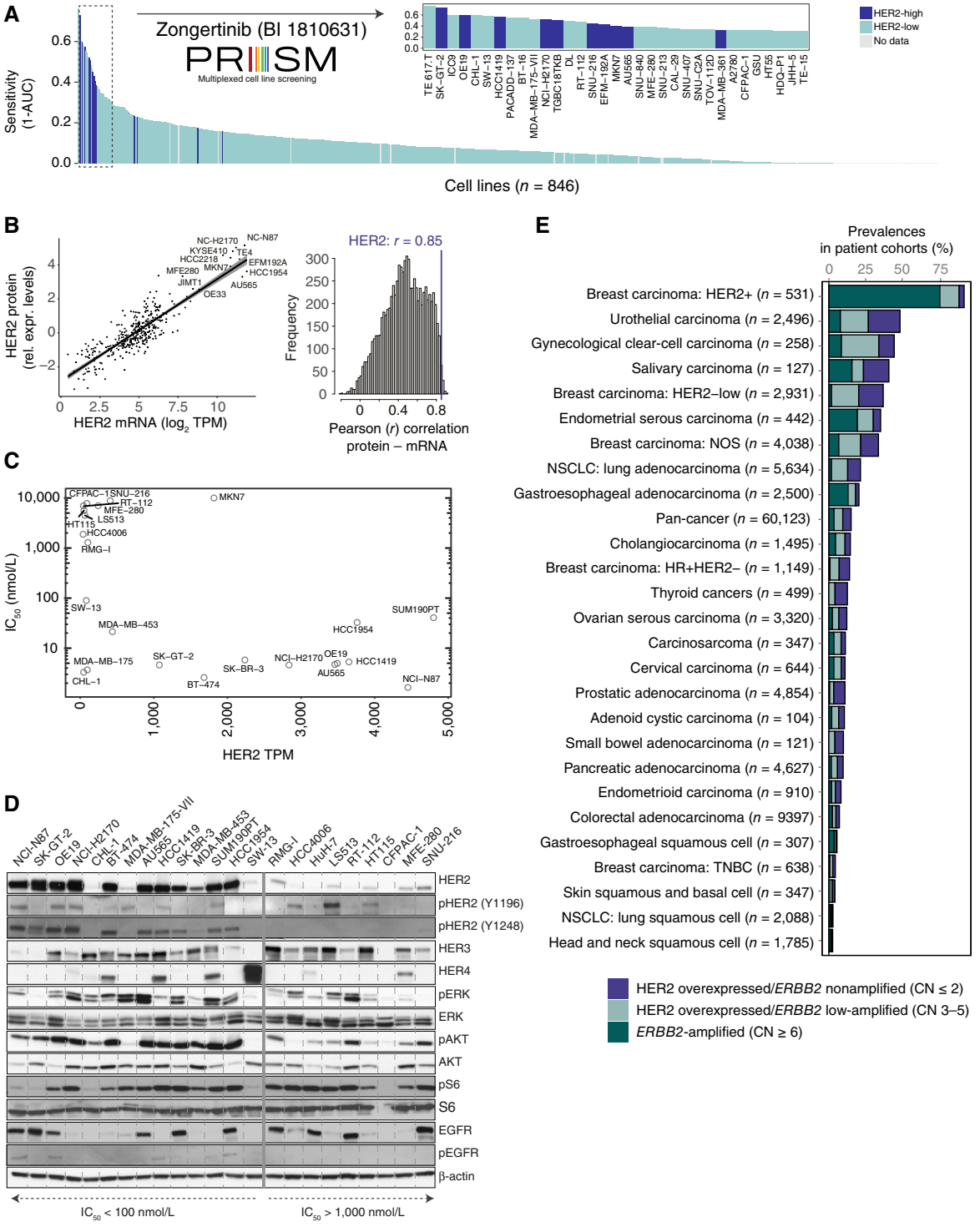

Figure 3. Zongertinib activity correlates with the HER2 status in cell lines. **A,** Sensitivity to zongertinib in 846 cancer cell lines color-coded by HER2 expression levels using a cutoff of ≥ TPM 250 (250 ; HER2-high). Cell lines are arranged from left to right in order of decreasing sensitivity to zongertinib. **B,** Correlation analysis of HER2 protein and mRNA levels in cancer cell lines (left). Proteome- and transcriptome-wide correlation analysis of protein and mRNA levels across cell lines. *X*-axis: Pearson correlation coefficients binned (right). **C,** Validation of PRISM screen in selected cancer cell lines spanning a spectrum of HER2 expression levels. *X*-axis: HER2 mRNA expression in TPM; *Y*-axis: IC_{50} in nmol/L (CellTiter-Glo assay). **D,** Western blot for the total and phosphorylated ERBB members and downstream mediators in indicated cell lines from **C** in untreated setting (baseline). Note: p-AKT (S473). **E,** Prevalence of HER2 amplifications and overexpression in indicated patient cohorts across a total of >60,000 tumor samples from Tempus AI pan-cancer gene expression records. A HER2 overexpression cutoff was computed using logistic regression on all HER2-amplified (CN ≥6) samples. Samples were then grouped by indication, and the prevalence of *ERRB2*-amplified, HER2-overexpressed/*ERBB2* low-amplified, and HER2-overexpressed/*ERBB2* nonamplified cases per cohort is visualized. Indications are ranked by the overall prevalence per cohort, and the number of cases in each cohort is indicated. CN, copy number; Dox, doxycycline; rel. expr., relative expression.

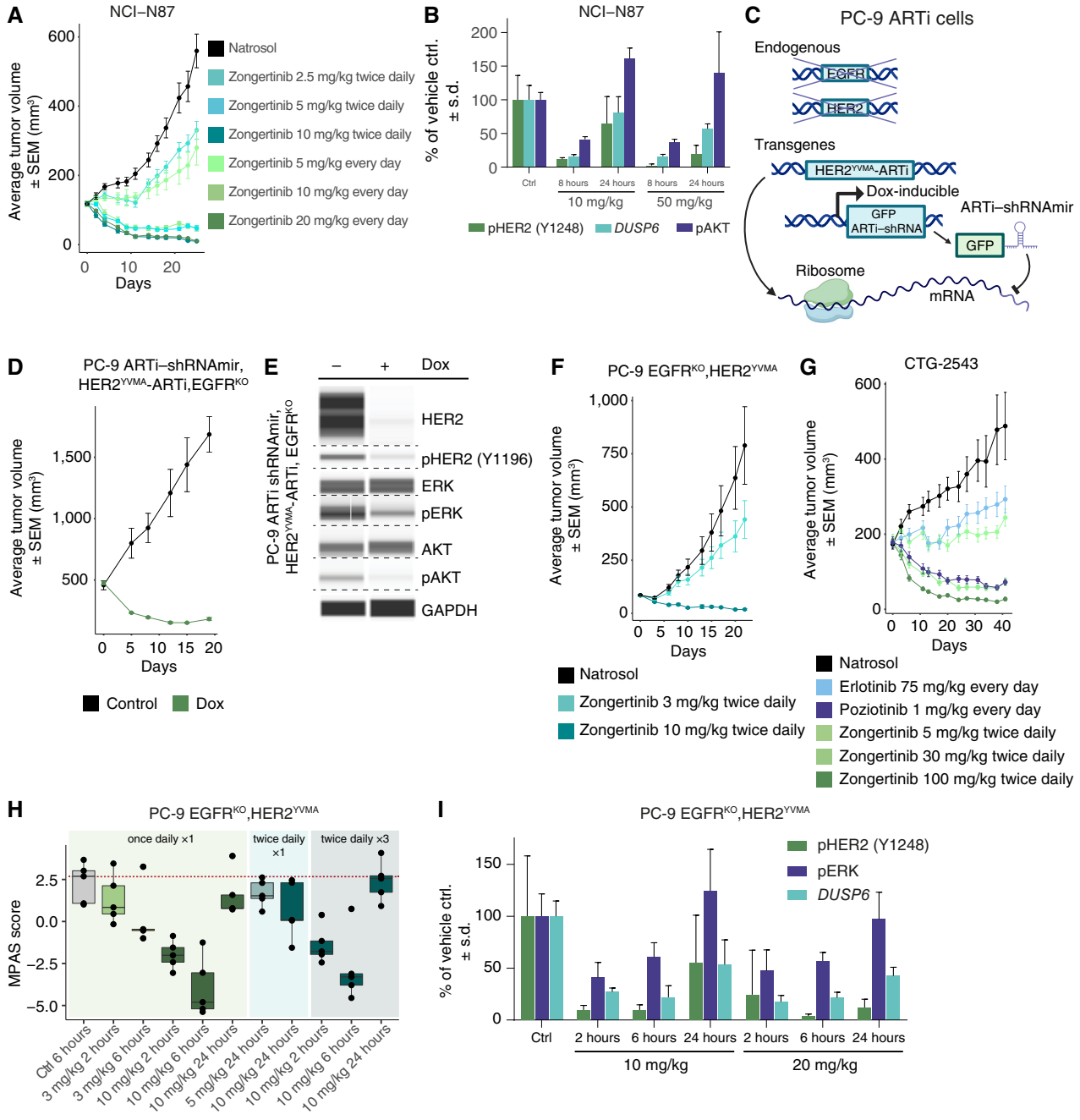

Figure 4. Zongertinib reduces tumor growth in preclinical models with different HER2 oncogenic mechanisms. **A,** Growth curves of tumors derived from HER2^{WT}-amplified NCI-N87 cells in mice treated with indicated doses and dosing schedules of zongertinib or the control natrosol. The mean tumor volume ± SEM is plotted for all *in vivo* experiments. **B,** Modulation of HER2 phosphorylation (ELISA), *DUSP6* expression (QuantSeq), and AKT phosphorylation (S473; ELISA) in mice engrafted with NCI-N87 tumors upon zongertinib treatment. Animals were dosed twice daily, 6 hours apart, for 3 days; timepoints are relative to the first dose on day 3. **C,** Schematic outline of the cell line engineering strategy. Endogenous *ERBB2* and *EGFR* were knocked out in PC-9 cells while overexpressing a HER2^{YVMA} construct containing an ARTi-RNAi target sequence. Knockdown is achieved by doxycycline-induced expression of an ARTi–shRNA coupled to GFP. **D,** *In vivo* experiment comparing doxycyclin-induced PC-9 EGFR^{KO},HER2^{YVMA}-ARTi knockdown to control treatment. **E,** Doxycycline-induced knockdown of HER2 in PC-9 EGFR^{KO},HER2^{YVMA}-ARTi cells and concurrent downmodulation of pERK and pAKT. **F,** Growth curves of tumors derived from PC-9 EGFR^{KO}, HER2^{YVMA} cells in mice treated with indicated doses and dosing schedules of zongertinib or the control natrosol. **G,** Growth curves of tumors derived from a PDX model (CTG-2543) carrying a HER2 exon 20 insertion (HER2^{YVMA}) treated with indicated doses of zongertinib, the EGFR inhibitor erlotinib, the pan-ERBB inhibitor poziotinib, or the control natrosol. **H,** Downregulation of MPAS gene signature in the PC-9 EGFR^{KO}, HER2^{YVMA} xenograft model upon zongertinib treatment. Each group contained up to five animals. Some groups show a lower number of replicates in the case the respective samples did not pass quality control. Dosing schemata (every day and twice a day) are highlighted on the figure. **I,** Modulation of HER2 phosphorylation (ELISA), DUSP6 expression (hybridization-based), and ERK phosphorylation (ELISA) in mice engrafted with PC-9 EGFR^{KO}, HER2^{YVMA} tumors upon zongertinib treatment. Animals were treated once per day with the indicated doses for 3 days, and timepoints are relative to the last dose. shRNA, short hairpin RNA.

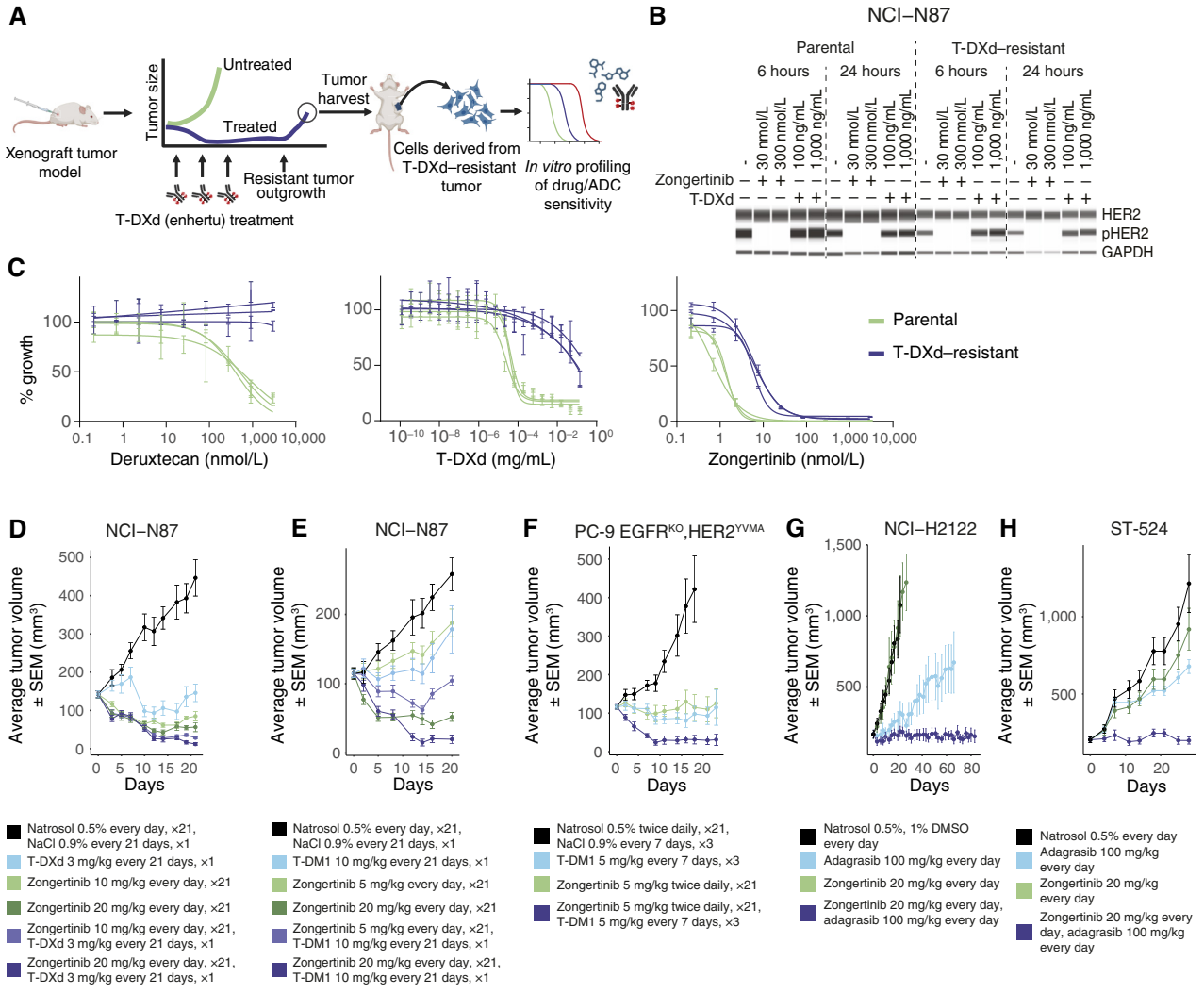

Figure 5. Zongertinib is a rational combination partner for HER2- and KRAS-targeted therapies. **A,** Schematic of the experiment for data in **B** and **C**. T-DXd–resistant tumors are generated *in vivo*, harvested, and cultured *in vitro* and then tested for sensitivities to T-DXd, the T-DXd payload deruxtecan, and zongertinib. **B,** Reduction of phosphorylated HER2 (Y1196) upon zongertinib but not T-DXd treatment in parental and T-DXd–resistant NCI-N87 cells. **C,** Dose–response curves (each line represents an independent experiment) of parental and T-DXd–resistant NCI-N87 cells to indicated treatments *in vitro*. **D,** Growth curves of tumors derived from NCI-N87 cells in mice treated with zongertinib or T-DXd individually or in combination. **E,** Growth curves of tumors derived from NCI-N87 cells in mice treated with zongertinib or T-DM1 individually or in combination. **F,** Growth curves of tumors derived from PC-9 EGFR^{KO},HER2^{YVMA} cells in mice treated with zongertinib or T-DM1 individually or in combination. **G,** Growth curves of tumors derived from NCI-H2122 cells in mice treated with zongertinib or adagrasib individually or in combination. **H,** Growth curves of tumors derived from ST-524, a KRAS^{G12C}-dependent but HER2-independent colorectal PDX, in mice treated with zongertinib or adagrasib individually or in combination.

We therefore investigated the combination potential. The TGI of NCI-N87 xenografts was assessed following administration of T-DXd, zongertinib, and their combination (Fig. 5D; Supplementary Fig. S7A). Single-agent treatment with T-DXd at 3 mg/kg shrank tumors, but tumors started to regrow at the end of the 21-day experiment. Tumors in mice treated with zongertinib at 10 or 20 mg/kg/day continuously shrank more than those in mice treated with T-DXd. Combining T-DXd with either dose of zongertinib resulted in greater tumor shrinkage than any single-agent treatment (Fig. 5D; Supplementary Fig. S7A). We then investigated whether combination with zongertinib would also improve the efficacy of T-DM1, another trastuzumab-based ADC that carries a different payload (Fig. 5E). T-DM1 at 10 mg/kg alone suppressed the growth of NCI-N87 tumors but did not shrink them. Zongertinib at 5 mg/kg/day also did not shrink tumors. Combining T-DM1 with zongertinib at 5 mg/kg/day reduced tumor size, but tumors regrew after 15 days. Consistent with the previous experiment, treatment with zongertinib at 20 mg/kg/day induced deep and persistent tumor shrinkage. Intriguingly, adding T-DM1 at 10 mg/kg to the first dosing of zongertinib at 20 mg/kg/day induced an even deeper response (Fig. 5E). In the mechanistic PC-9 EGFR^{KO}, HER2^{YVMA} tumor model, T-DM1 at 5 mg/kg once or zongertinib at 5 mg/kg/day (monotherapies) abolished tumor growth, whereas the combination of T-DM1 and zongertinib unexpectedly induced persistent tumor shrinkage (Fig. 5F).

Increased ERBB signaling has been suggested to act as a resistance mechanism to $KRAS^{G12C}$ inhibitors (58). However, it was not predictable how an $EGFR^{WT}$-sparing, HER2-selective inhibitor would perform in combination with KRAS G12C inhibitors. We therefore investigated if adding zongertinib to $KRAS^{G12C}$ inhibitors could enhance the efficacy and/or reduce resistance (Fig. 5G and H; Supplementary Fig. S7B and S7C). We tested this using the NCI-H2122 xenograft model, which expresses $KRAS^{G12C}$ and is dependent on $KRAS^{G12C}$ but not HER2 (Fig. 5G). As expected, zongertinib monotherapy did not affect the growth of these tumors. Both sotorasib and adagrasib reduced, but did not prevent, tumor growth (Fig. 5G; Supplementary Fig. S7B). Adding zongertinib to sotorasib further suppressed tumor growth, whereas adding zongertinib to adagrasib persistently abolished tumor growth (Fig. 5G; Supplementary Fig. S7B). We further tested the potential of combining zongertinib with KRAS inhibitors using the colorectal ST-524 PDX model that expresses $KRAS^{G12C}$. A combination of zongertinib and adagrasib shrank tumors, whereas neither agent alone achieved this (Fig. 5H). In agreement with this, adagrasib achieved tumor stasis in the lung cancer ST-4341 $KRAS^{G12C}$ PDX model, with signs of outgrowth beyond day 50. The combination treatment of zongertinib and adagrasib deepened the response and achieved tumor regression beyond day 60 (Supplementary Fig. S7C). Overall, these data suggest a synergistic effect for combined HER2 and $KRAS^{G12C}$ inhibition.

Clinical trial 1479-0001 (NCT04886804) is a two-part phase I study of zongertinib in patients with advanced or metastatic solid tumors having confirmed HER2 aberrations, including HER2 overexpression, *ERBB2* gene amplification, nonsynonymous somatic *ERBB2* mutations, or gene rearrangements of either *ERBB2* or *NRG1*. Part Ia was a dose-escalation study with the objectives of investigating the safety, tolerability, and PK of escalating doses of zongertinib as monotherapy (administered orally twice a day or every day) in patients with advanced and/or metastatic solid tumors of any histology and of determining the MTD and/or the recommended phase II dose. Zongertinib showed early signs of clinical efficacy and good tolerability. During phase Ia (n = 61), two dose-limiting toxicities [platelet decrease G3 (360 mg every day) and diarrhea G3 (240 mg every day)] were noted, and at data cut-off (September 29, 2023), the MTD was not reached. Treatment-related AEs (TRAE) occurred in 72% of the patients (G3/G4/G5 with 10%/0%/0%, respectively). Serious TRAEs were observed in 2% (n = 1; G3 AST/ALT) of the patients. In 53 evaluable patients, the ORR and disease control rate (DCR) were 49% and 91%, respectively. In patients with HER2 mutations (n = 29), the ORR and DCR were 62% and 97%, respectively. In 36 evaluable patients with NSCLC, the ORR and DCR were 58% and 97%, respectively. The overall median duration of response was 12.7 months (95% CI, 4.2–12.7; ref. 59). Consistent with the preclinical tolerability data, zongertinib was well tolerated, with low rates of EGFR-mediated AEs. This study, including the dose expansion phase in various populations of patients with NSCLC with HER2 mutations, will be fully reported at maturity of the data. Based on the encouraging efficacy and tolerability data from NCT04886804, a phase III confirmatory study is underway (60).

As described above, zongertinib showed early signs of efficacy during phase Ia, and three case studies of patients without NSCLC histology and different oncogenic mechanisms are illustrated here (Fig. 6A–C). Patient 1 with stage IV cholangiocarcinoma characterized by a SDC4–NRG1 fusion had hepatectomy and received five lines of systemic treatments before entering the trial. The patient received zongertinib at 60 mg every day and achieved partial response (PR) after two cycles of treatment. Consistently, the level of the blood tumor marker carbohydrate antigen 19-9 decreased upon treatment with zongertinib (Fig. 6A). Patient 2 had stage IV breast adenocarcinoma that was confirmed to have a HER2 mutation (2329G>T p.Val777Leu, variant allele frequency (VAF) 44%) V777L in exon 20 and PIK3CA H1047L comutation (variant allele frequency 37%). The patient received several lines of chemotherapy and hormonal therapy, including fulvestrant and palbociclib, before entering the study. The patient received zongertinib at 360 mg every day and achieved PR after two cycles of treatment. Consistently, the cancer antigen marker 15-3 decreased (Fig. 6B). The patient has an ongoing response in its sixth treatment cycle and tolerates the treatment well. The third patient (Fig. 6C) is a 65-year-old woman with stage IV *ERBB2* gene–amplified breast cancer. Before entering the study, she received six lines of therapies, including chemotherapy, combined with multiple HER2-targeted agents (pertuzumab/trastuzumab, capecitabine/trastuzumab, T-DM1, vinorelbine, T-DXd and Teysuno/tucatinib/trastuzumab). The patient received zongertinib in the seventh line at a daily dose of 300 mg and achieved PR on the second cycle, which lasted for a total of 10 cycles. Treatment was well tolerated, with grade 1 diarrhea as the only side effect.

Together, these three cases demonstrate that zongertinib can induce tumor regressions in heavily pretreated patients suffering from tumors that display relevant HER2 aberrations and that anecdotal clinical activity was also observed beyond NSCLC. The clinical activity of zongertinib was observed in early escalation steps in which patients also received lower doses than the two doses (120 and 240 mg every day) tested for dose optimization.

DISCUSSION

Our data show that zongertinib is a promising treatment option for patients with HER2-dependent cancers. Zongertinib covalently inhibits HER2 with high potency and selectivity across a large panel of kinases, including $EGFR^{WT}$. In cell proliferation assays, zongertinib potently inhibits the proliferation of not only Ba/F3 cell models dependent on $HER2^{WT}$ or on various HER2 mutants but also human cancer cell lines dependent on HER2, including those expressing NRG1 fusions, $HER2^{YVMA}$ and other mutations, and high levels of $HER2^{WT}$. Of note, much higher concentrations of zongertinib are required to inhibit the proliferation of Ba/F3 cell models and human cancer cell lines not dependent on HER2, including those dependent on $EGFR^{WT}$. The sensitivity of a large panel of human cancer cell lines toward zongertinib correlates with $HER2^{WT}$ expression levels. These results demonstrate that selective pharmacological inhibition of HER2 mirrors the results of genetic inhibition of HER2, observed in large-scale CRISPR-Cas9 and RNAi screens (61–64).

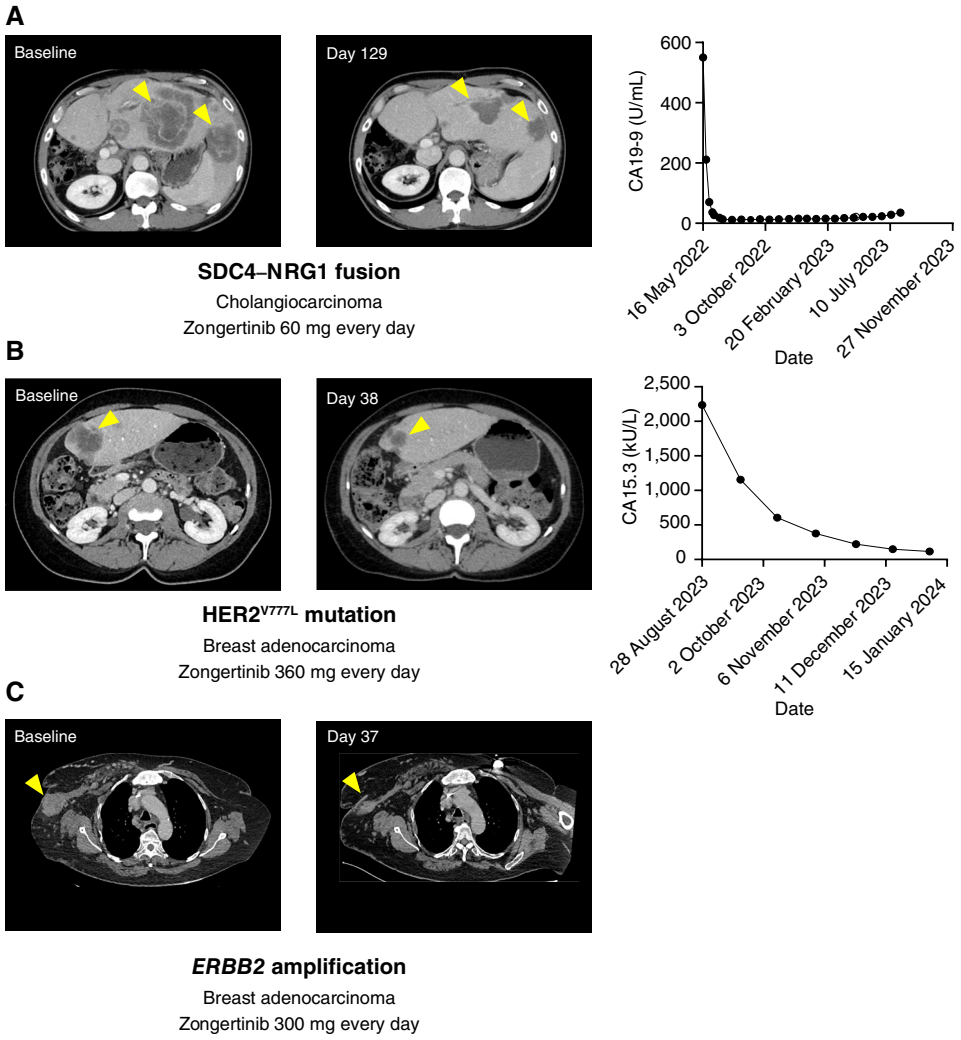

Figure 6. Zongertinib reduces tumor burden in patients. **A,** Pre- and on-treatment CT scans of a patient having stage IV cholangiocarcinoma (baseline panel) with a SDC4–NRG1 fusion treated with zongertinib and showing a response (day 129 panel). Quantification of the tumor marker CA19-9 in the blood at indicated dates (x-axis; right). **B,** Pre- and on-treatment CT scans of a patient having stage IV breast cancer (baseline panel) with a HER2^{V777L} exon 20 mutation treated with zongertinib and showing a response at the first evaluation (day 38 panel). Quantification of the tumor marker CA15.3 in the blood at indicated dates (x-axis; right). **C,** Pre- and on-treatment CT scans of a patient having stage IV breast cancer (baseline panel) with *ERBB2* amplification treated with zongertinib and showing a tumor response of the locoregional recurrence (right axilla) at the first evaluation (day 37 panel). No biomarker data are available for this patient.

In vivo, single-agent zongertinib treatment inhibits the growth and reduces the size of tumors in cell line–derived (HER2^{WT}-high expression or HER2^{YVMA}-dependent) and PDX (HER2^{YVMA} dependent) models.

Consistent with *in vitro* biochemical assay results and cell proliferation results, zongertinib treatment time- and dose-dependently downregulates phosphorylated HER2, as well as downstream MAPK and PI3K signaling pathways, in cells dependent on HER2. Zongertinib treatment reduces not only the level of phosphorylated ERK but also the expression of ERK target genes, such as DUSP6, SPRY4, ETV4, ETV5, and FOSL1. Consistent with the selectivity of zongertinib in biochemical assays in inhibiting HER2 over EGFR^{WT}, considerably higher doses are required to reduce EGFR phosphorylation levels in an EGFR^{WT}-dependent cell line.

Zongertinib binds the ATP-binding site of HER2 and forms a covalent bond with cysteine 805. As demonstrated in this study, this covalent binding of HER2 is critical for the high potency of zongertinib in inhibiting cell proliferation. This mechanism of action of zongertinib is clearly different from that of T-DM1 and T-DXd. Although both ADCs rely on trastuzumab to bind to HER2-expressing cells, they differ in the attached cytotoxic moiety. T-DM1 utilizes a microtubule inhibitor, whereas T-DXd utilizes a topoisomerase I inhibitor. Using a cell line model, we demonstrate that zongertinib combines well with HER2-directed ADCs and potently inhibits the proliferation of HER2-dependent cells that have acquired resistance to T-DXd. In a HER2-dependent xenograft model, we show that adding zongertinib enhances the antitumor activity of T-DXd and T-DM1. The data presented in this

study raise the exciting possibility that zongertinib may be effective in treating HER2-dependent tumors that are resistant to these ADCs and indicate that adding zongertinib may expand the population of patients who would benefit from HER2-targeting ADCs.

A recent exciting development in the treatment of patients with NSCLC is the approval of $KRAS^{G12C}$ inhibitors sotorasib and adagrasib to treat patients whose tumors express $KRAS^{G12C}$, which account for about 13% of NSCLC cases. KRAS is a major downstream mediator of ERBB signaling. Preclinical studies have shown that cotargeting an oncogenic KRAS mutant with EGFR more potently inhibits cells dependent on that KRAS mutant than targeting the KRAS mutant alone (58), leaving room to speculate if selective inhibition of other ERBB members would result in a synergistic combination effect. We demonstrate in this study that zongertinib inhibits the growth of a $KRAS^{G12C}$-dependent xenograft model synergistically with both sotorasib and adagrasib and that a combination of zongertinib with adagrasib induces persistent tumor shrinkage in a PDX model, whereas neither alone can induce this effect.

Our clinical data confirm the preclinical hypothesis that selective HER2 inhibition while sparing $EGFR^{WT}$ can permit doses in patients, with evidence of activity in patients with tumors with aberrant HER2 activation, either through expression of a ligand fusion reported to signal through HER2 or expression of an oncogenic HER2 mutant or aberrantly high levels of HER2. A manuscript describing the clinical results of a dose expansion clinical trial is currently in preparation for publication.

In summary, our study indicates that zongertinib is a promising treatment option for patients with HER2-dependent solid cancers as monotherapy and as concurrent treatment with ADC therapy or with KRAS-targeted drugs.

METHODS

Synthesis of Zongertinib (N-(1-(8-((3-methyl-4-((1-methyl-1H-benzo[d]imidazol-5-yl)oxy)phenyl)amino)pyrimido[5,4-d]pyrimidin-2-yl)piperidin-4-yl)acrylamide)

An overview of the synthetic routes to zongertinib and BI-3999 is shown in Supplementary Fig. S1, and graphical NMR spectra are shown in Supplementary Fig. S2.

3-methyl-4-((1-methyl-1*H*-benzo[*d*]imidazol-5-yl)oxy)aniline (500 mg, 1.97 mmol) and 8-chloro-2-(methylthio)pyrimido[5,4-*d*]pyrimidine hydrochloride (492 mg, 1.97 mmol) were suspended in isopropanol, and the resulting reaction mixture stirred at 50°C for 3 hours, at which time high-performance liquid chromatography–mass spectrometry (HPLC-MS) indicated full conversion. The reaction mixture was concentrated under reduced pressure, and the crude product was redissolved in dichloromethane and washed with aqueous $NaHCO_3$. The organic layer was dried over Na_2SO_4 and concentrated, and the resulting crude product was purified by column chromatography (SiO_2, gradient of 0%–15% methanol in dichloromethane) to afford the product (840 mg).

N-(3-methyl-4-((1-methyl-1*H*-benzo[*d*]imidazol-5-yl)oxy)phenyl)-6-(methylthio)pyrimido[5,4-*d*]pyrimidin-4-amine (860 mg, 90%, 1.80 mmol) was suspended in dichloromethane (30 mL), and the resulting mixture was cooled to 0°C to 5°C. mCPBA (3-chloroperbenzoic acid, 444 mg, 77%, 1.98 mmol) was added portionwise over 1 hour, and the resulting reaction mixture was stirred at room temperature overnight, at which time HPLC-MS indicated full conversion. The reaction mixture was diluted with dichloromethane and washed with aqueous $NaHCO_3$. The organic layer was dried over Na_2SO_4 and concentrated, and the resulting crude product which was used directly in the next step (767 mg, crude).

N-(3-methyl-4-((1-methyl-1*H*-benzo[*d*]imidazol-5-yl)oxy)phenyl)-6-(methylsulfinyl)pyrimido[5,4-*d*]pyrimidin-4-amine (5.42 g, 80%, 9.73 mmol) was dissolved in *N*,*N*-dimethyl formamide (DMF, 50 mL) and diisopropylethylamine (2.8 mL, 16 mmol). 4-*Boc*-amino-1-piperidine (2.39 g, 11.9 mmol) was added, and the reaction was stirred at 60°C overnight. Then, the reaction mixture was concentrated, and the crude product was used directly in the next step (5.66 g, crude).

Tert-butyl (1-(8-((3-methyl-4-((1-methyl-1*H*-benzo[*d*]imidazol-5-yl)oxy)phenyl)amino)pyrimido[5,4-*d*]pyrimidin-2-yl)piperidin-4-yl)carbamate (5.66 g, 9.73 mmol) was dissolved in dichloromethane (100 mL) and methanol (30 mL). Four mol/L HCl in dioxane (11 mL, 44 mmol) was added, and the resulting reaction mixture was heated to 45°C for 7 hours. HPLC-MS indicated some remaining starting material; therefore, the reaction mixture was stirred at room temperature overnight. Four mol/L HCl in dioxane (1 mL, 0.40 mmol) was added, and the reaction mixture was reheated to 45°C for 4 hours, at which time HPLC-MS indicated full conversion. The reaction mixture was concentrated, and the resulting crude product was purified by column chromatography (SiO_2, gradient of 0%–20% methanol in dichloromethane) to afford the product (4.5 g, 70% purity).

1-[8-({3-methyl-4-[(1-methyl-1*H*-1,3-benzodiazol-5-yl)oxy]phenyl}amino)-[1,3]diazino[5,4-*d*]pyrimidin-2-yl]piperidin-4-amine (4.5 g, 70%, 6.9 mmol) was suspended in dichloromethane (150 mL) and triethyl amine (4 mL, 28 mmol), and dimethylaminopyridine (115 mg, 0.941 mmol) was added. Then, acroyloyl anhydride (1.36 g, 95%, 10.3 mmol) was added, and the resulting reaction mixture was stirred at room temperature for 1 hour, at which time HPLC-MS indicated full conversion. The reaction mixture was diluted with dichloromethane (50 mL) and washed with aqueous $NaHCO_3$ and brine. The organic layer was dried over Na_2SO_4 and concentrated, and the resulting crude product was purified by column chromatography (SiO_2, gradient of 0%–20% methanol in dichloromethane) to afford the product (2.49 g).

^{1}H NMR (DMSO-d_6, 500 MHz) δ 9.58 (s, 1H), 9.08 (s, 1H), 8.39 (s, 1H), 8.19 (s, 1H), 8.10 (d, 1H, J = 7.6 Hz), 7.84 (d, 1H, J = 2.2 Hz), 7.77 (dd, 1H, J = 8.8 Hz, J = 2.2 Hz), 7.57 (d, 1H, J = 8.8 Hz), 7.09 (d, 1H, J = 2.2 Hz), 7.00 (dd, 1H, J = 2.2, 8.5 Hz), 6.89 (d, 1H, J = 8.8 Hz), 6.20 (dd, 1H, J = 10.1, 17.0 Hz), 6.10 (dd, 1H, J = 2.2, 17.0 Hz), 5.6 (dd, 1H, J = 2.2, 9.8 Hz), 4.86 (m, 2H), 3.99 (m, 1H), 3.84 (s, 3H), 3.25 (m, 2H), 2.26 (s, 3H), 1.92 (m, 2H), and 1.43 (m, 2H).

Synthesis of BI-3999 (N-(1-(8-((3-methyl-4-((1-methyl-1H-benzo[d]imidazol-5-yl)oxy)phenyl)amino)pyrimido[5,4-d]pyrimidin-2-yl)piperidin-4-yl)acetamide)

6-(4-aminopiperidin-1-yl)-*N*-(3-methyl-4-((1-methyl-1*H*-benzo[*d*]imidazol-5-yl)oxy)phenyl)pyrimido[5,4-*d*]pyrimidin-4-amine (100 mg, 208 mmol) and 4-dimethylaminopyridine (2.5 mg, 0.02 mmol) were suspended in 5 mL dichloromethane. Acetic anhydride (25 µL, 0.23 mmol) was added, and the resulting reaction mixture was stirred at room temperature for one hour. Then, the reaction mixture was diluted with dichloromethane and washed with aqueous $NaHCO_3$ and brine. Then, the layers were separated, and the organic layer was dried over $MgSO_4$ and concentrated. The crude product was purified by column chromatography (SiO_2, gradient of 0%–10% methanol in dichloromethane) to afford the product (75 mg).

^{1}H NMR (DMSO-d_6, 400 MHz) δ 9.58 (s, 1H), 9.07 (s, 1H), 8.39 (s, 1H), 8.17 (s, 1H), 7.88 (d, 1H, J = 7.9 Hz), 7.84 (d, 1H, J = 2.5 Hz), 7.77 (dd, 1H, J = 2.7, 8.7 Hz), 7.57 (d, 1H, J = 8.9 Hz), 7.09 (d, 1H, J = 2.3 Hz), 7.00 (dd, 1H, J = 2.3, 8.6 Hz), 6.89 (d, 1H, J = 8.6 Hz), 4.85 (m, 2H), 3.90 (m, 1H), 3.84 (s, 3H), 3.23 (m, 2H), 2.26 (s, 3H), 1.88 (m, 2H), 1.82 (s, 3H), and 1.38 (m, 2H).

Kinase Panel

Kinase selectivity was investigated using the Thermo Fisher Scientific SelectScreen kinase profiling services measuring single-point inhibition at 1 μmol/L for a broad panel of kinases and dose–response curves for selected kinases.

Cell Lines

Cell lines used for cell proliferation assays and immunoblots were obtained from the American Type Culture Collection (ATCC) (AU565, BT-474, CFPAC-1, CHL-1, HCC1419, HCC1954, HCC4006, LS513, MDA-MB-175-VII, MDA-MB-453, NCI-H2170, NCI-N87, SK-BR-3, and SW-13), European Collection of Animal Cell Cultures (ECACC) (HT115), Japanese Collection of Research Bioresources Cell Bank (JCRB) (HuH-7, MKN7, and RMG-I), Deutsche Sammlung von Mikroorganismen und Zellkulturen (DSMZ) (MFE-280, OE19, RT-112, and SK-GT-2), Korean Cell Line Bank (KCLB) (SNU-216), or Arterand (SUM190PT) and cultivated according to the suppliers' recommendations, except for MDA-MB-175-VII. All cell lines were *Mycoplasma*-tested and validated by next-generation sequencing (NGS) and short tandem repeat profiling (STR). Master cell banks were made upon purchasing individual lines, and fresh aliquots were used for the experiments. For proliferation assays and immunoblots shown in Fig. 3C and D, MDA-MB-175-II cells were kept under suppliers' recommendations for all other assays. MDA-MB-175-VII cells were cultivated at 37°C and 5% CO_2 in DMEM (Sigma-Aldrich, D4629) supplemented with 10% FBS (Gibco, 26140079), GlutaMAX (Gibco, 35050038), and sodium pyruvate (Gibco, 11360039). Ba/F3 cell lines were generated as described previously (49). PC-9 $HER2^{YVMA}$ ARTi cell lines were generated as previously described for the $EGFR^{del19}$ variant (56) using a pMSCV-driven $HER2^{YVMA}$-dsRed-ARTi construct. Knockdown was induced with doxycycline in the drinking water (2 mg/mL with 2% Sucrose). ARTi studies were conducted in NMRI-*Foxn1nu* mice.

Proliferation Assay

Cells were seeded in white, sterile 96-well or 384-well culture plates (white with white flat bottom, TC-treated; PerkinElmer, #6005680 or #6007680). In general, seeded cells were incubated overnight in a humidified incubator at 37°C and 5% CO_2; exceptions were MDA-MB-453 and SW-13, which were grown at 37°C but without CO_2. 0.1% DMSO–control or serial compound dilution in triplicates was added. After 5 days of incubation with test compounds, the cells plates were measured upon the addition of CellTiter-Glo Luminescent Cell Viability Reagent (Promega, Cat. No. G9243) to assess cell viability. The plates were placed on a shaker for 5 minutes and additionally incubated for 10 minutes at room temperature to induce cell lysis and to stabilize the luminescent signal. The luminescent signal of each well was measured using an EnSpire or EnSight multilabel plate reader (PerkinElmer). The IC_{50} values were calculated using Boehringer Ingelheim's proprietary software MegaLab, and curve fitting was based on the program PRISM, GraphPad Inc.

Immunoblots

Logarithmically growing cells were harvested and lysed, 14 μg total protein was loaded per lane, and gels were transferred to PVDF membranes (Bio-Rad, #1704157) after saturation of membranes with 5% milk in TBS-T. The following primary antibodies were added [all antibodies were obtained from Cell Signaling Technology, HER2 (#4290)]: pHER2 [#6942 (p-Y1196) or #2247 (p-Y1248)], HER3 (#12708), HER4 (#4795), pERK (#4370), ERK (#9102), pAKT (#4058), AKT (#9272), and beta-Actin (#4967). Goat anti-rabbit horseradish peroxidase–linked antibody was obtained from Dako (#P0448). Enhanced chemiluminescence signal (using GE Healthcare, #RPN2106, or Merck, #64-202BP) was detected using X-ray films.

Simple Western Capillary Immunoassay

A total of 1×10^5 cells were plated per well in a 24-well plate. The next day, the cells were treated with zongertinib, poziotinib, or T-DXd for 6 hours. The cells were then washed with 1 mL of PBS and lysed with 50 μL with RIPA lysis buffer (R2078, Sigma-Aldrich) supplemented with HaltTM proteinase inhibitor cocktail (1:100, Thermo Fisher Scientific, 78438) and 0.25 μL Benzonase nuclease (Millipore, 70746). Four μL of lysate was taken for Western (WES) analysis using 12 to 230 kDa Separation Module (ProteinSimple, SM-W004). The following antibodies were used: HER2 (1:100, Cell Signaling Technology, 4290), pHER2-Tyr1196 (1:100, Cell Signaling Technology, 6942), EGFR (1:100, Cell Signaling Technology, 4267), pEGFR- Tyr1068 (1:100, Cell Signaling Technology, 3777), ERK 1/2 (1:100, Cell Signaling Technology, 9102), pERK 1/2 -Thr202/Tyr204 (1:100, Cell Signaling Technology, 4370), AKT (1:100, Cell Signaling Technology, 9272), pAKT–Ser473 (1:100, Cell Signaling Technology, 4060), DUSP6 (1:100, Abcam, ab76310), S6 (1:100, Cell Signaling Technology, 2217), pS6 –Ser235/236 (1:100, Cell Signaling Technology, 2211), and GAPDH (1:300, Abcam, ab9485). WES data were analyzed using Compass for SW software (v6.1.0, ProteinSimple).

Phosphoprotein In Vivo Biomarker Analyses

pERK and pHER2 modulations in tumors were determined using the phospho/total ERK1/2 (Meso Scale Diagnostics, K15107D) or phospho (Tyr1248)/total ErbB2 (Meso Scale Diagnostics, K15125D) whole-cell lysate kits, respectively, as recommended by the manufacturer. Briefly, tumors were homogenized in lysis buffer (Meso Scale Discovery, product code R60TX-2) supplemented with 1:100 phosphatase inhibitor cocktail #2 (Sigma-Aldrich, product code P5726), phosphatase inhibitor cocktail #3 (Sigma-Aldrich, product code P0044), protease inhibitor cocktail (Roche, product code 11836170001), 1 mmol/L phenylmethanesulfonyl fluoride (Sigma-Aldrich, product code P7626), and 0.1% SDS (Sigma-Aldrich, product code 75746) using ReadyPrep mini grinders (Bio-Rad, product code 163-2146) and resin tubes (Bio-Rad, product code 163-2146) as recommended by the manufacturer. Lysates were cleared by centrifugation (10 minutes, 10,000 × *g*) and analyzed using a MESO SECTOR S 600 reader (Meso Scale Discovery).

Gene Expression In Vivo Biomarker Analyses

For *DUSP6* modulation in tumors, RNA was isolated using RNeasy Mini Kit (Qiagen, product code 73404). Less than 50 mg tumor (typically around 10 mg) was homogenized in 900 μL QIAzol lysis reagent using a TissueLyser II device (Qiagen, 1 minute, 30 Hz), adding a 5-mm stainless steel bead per tube. All further steps of RNA purification were carried out as specified by the manufacturer using 1-bromo-2-chloropropane (Sigma-Aldrich, product code B9673) instead of chloroform. RNA samples were analyzed using QuantiGene Singleplex Assay Kit (Invitrogen, product code QS0013) and Singleplex RNA probes (Invitrogen, product code QGS-200; assay IDs SA-11958 for *DUSP6* and SA-10057 for *TBP* as a housekeeping gene). Alternatively, RNA was analyzed by reverse transcription and sequencing as detailed below.

Solubility

Solubility measurement of zongertinib was conducted using the shake flask method. Samples up to a compound concentration of ~1 mg/mL were shaken in the respective solvent for 2 hours at room temperature. After filtrating the samples, the compound concentration in the filtrate was determined using HPLC-UV.

Determination of Bidirectional Permeability in MDCK-MDR1 and MDCK-BCRP Cells

Assessment of bidirectional permeability was conducted as described previously (65, 66) using MDCK-MDR1 and MCKD-BCRP cells instead of Caco-2 cells. Briefly, after reconstitution in culture media, assay-ready frozen cells were seeded onto Transwell inserts (#3379, Corning). The cells were cultured at 37°C and 95% relative humidity in the presence of 5% CO_2 for 9 to 10 days. For permeability assessment, the compounds were diluted in transport buffer (128.13 mmol/L NaCl, 5.36 mmol/L KCl, 1 mmol/L $MgSO_4$, 1.8 mmol/L $CaCl_2$, 4.17 mmol/L $NaHCO_3$, 1.19 mmol/L Na_2HPO_4, 0.41 mmol/L NaH_2PO_4, 15 mmol/L 2-[4-(2-hydroxyethyl)piperazin-1-yl]ethanesulfonic acid, 20 mmol/L glucose, pH 7.4, and 0.25% BSA) at a final compound concentration of 10 µmol/L. The incubation solution was added to the apical or basal donor compartment, and transport buffer without test compounds was added to the opposite receiver compartment and incubated for up to 2 hours. Samples were taken at different time points, followed by test compound concentration quantification by LC-MS/MS. Apparent permeability coefficients ($P_{app,AB}$, $P_{app,BA}$) were calculated as follows:

$$P_{app,AB} = \frac{Q_{AB}}{C_0 \times s \times t}$$

$$P_{app,BA} = \frac{Q_{BA}}{C_0 \times s \times t}$$

in which Q is defined as the amount of compound recovered in the receiver compartment after the incubation time t, C_0 as the initial compound concentration given to the donor compartment, and s as the surface area of the Transwell inserts. The efflux ratio is calculated as the quotient of $P_{app,BA}$ to $P_{app,AB}$ (each mean of duplicates). In both cell types, one reference compound (apafant in MDCK-MDR1 and daizein for MDCK-BCRP) as well as a low-permeable compound (BI internal reference, $P_{app} \approx 3 \times 10^{-7}$ cm/seconds, no efflux) were included as assay controls. The different references, as well as transepithelial electrical resistance measurements before the permeability assay, were used to ensure the quality of the assays.

Assessment of Plasma Protein Binding In Vitro

Binding of research compounds to plasma protein was determined using the equilibrium dialysis method, as described previously (67). Briefly, plasma of different species was spiked with 3 µmol/L (1% v/v DMSO) of the test compound and dialyzed in equilibrium dialysis cells (RED-device, Thermo Fisher Scientific) against 100 mmol/L potassium phosphate buffer, pH 7.4, for up for 5 hours at 37°C through a semipermeable membrane. After the incubation, donor and acceptor compartments were precipitated, and the compound concentrations were determined by HPLC-MS/MS. Calibration and quality control samples were prepared using blank plasma and the internal standard. The fraction unbound (f_u) is calculated as the ratio of the compound concentration in the acceptor compartment to the concentration in the donor compartment using technical triplicates.

Assessment of Metabolic Stability in Hepatocytes In Vitro

The metabolic stability kinetics of the test compound was assessed in a hepatocyte suspension assay. Briefly, 1 µmol/L test compound (at a final DMSO concentration of 0.05% v/v) was incubated in the presence of 1 Mio cells/mL at 37°C and 5% CO_2 in a humidified incubator. Samples were taken at six different time points up to 4 hours. Reactions were terminated by the addition of acetonitrile, and precipitates were separated by centrifugation. The compound concentration in supernatants was determined by HPLC-MS/MS, and clearance was calculated from compound half-lives using the well-stirred liver model. In each species incubation, two different references (one low- and one high-stability reference), as well as a cell-free chemical stability quality control, were included and used to ensure the quality of the assays.

Prediction of Human PK and Therapeutic Dose

PK data (i.v. and oral administration) determined in mouse, rat, dog, and minipig models were used to predict human PK properties of zongertinib (see Supplementary Fig. S1B).

Human clearance was predicted based on the *in vitro/in vivo* correlation using *in vitro* hepatocyte data and *in vivo* clearance data after i.v. administration, according to the following equation:

$$Cl = a * Cl_{in\ vivo,\text{predicted}} + b$$

in which Cl is the total body plasma clearance in human, $Cl_{in\ vivo,\text{predicted}}$ is the predicted hepatic metabolic blood clearance from *in vitro* data, and a and b are the parameters obtained from the regression analysis of the clearance values across multiple species.

Human V_{ss} was predicted based on the mean of the measured animal V_{ss} values corrected for species-dependent plasma–protein binding.

Oral bioavailability (F) was calculated using the average of the measured animal data. The absorption rate constant (k_a) was predicted as the mean k_a values from mouse, rat, dog, and minipig models. The k_a values of the different species were determined by fitting the animal data to a one-compartment PK model with first-order oral absorption, no lag time, and first-order elimination.

The predicted human dose for zongertinib was derived from a quantitative PK/TGI model. This preclinical semi-mechanistic mathematical model was built using input data from *in vitro* assessment as well as *in vivo* data from the PC-9 HER2^{YVMA} xenograft efficacy experiments. Compound plasma exposure and respective TGI data generated in mice were used to train the quantitative model. The PK/TGI model has consistently and reliably predicted tumor growth kinetics in the PC-9 HER2^{YVMA} xenograft models upon treatment with zongertinib. The PK/TGI model was used to identify the required dose administered in mouse to achieve tumor regressions in the PC-9 HER2^{YVMA} xenograft model. Likewise, the human PK plasma profile of zongertinib was simulated as a one-compartmental PK model using the predicted human PK parameters. Predicted exposures have been further incorporated into the PK/TGI model to estimate the required dose required to achieve a TGI >100% in both every day as well as twice a day dosing regimens.

NGS Library Preparation and Sequencing for Gene Expression Profiling

Cell derived RNA samples were normalized to 100 ng/µL in 10 µL nuclease-free H_2O. A measure of 500 ng of total RNA was used as the contribution for genome-wide gene expression profiling by 3′ mRNA sequencing. NGS libraries were prepared using QuantSeq 3′mRNA-Seq V2 Library Prep Kit FWD for Illumina (Lexogen GmbH) according to the manufacturer's protocol using the Biomek i7 automated liquid handling workstation (Beckman Coulter GmbH). After quality control by High Sensitivity D1000 ScreenTape on a 4200 TapeStation System (Agilent Technologies Österreich GmbH), individual libraries were normalized, equimolarly pooled, quantified using NEBNext Library Quant Kit for Illumina (New England BioLabs Inc., #E7630L), and sequenced on a NextSeq 2000 or NovaSeq 6000 instrument (Illumina) using 75 bp single-read chemistry.

Gene Expression Profiling (RNA-Seq) and Differential Gene Expression Analysis

See the methods section of 49.

Clinical Data

Written informed consent was obtained from all patients. Studies were conducted in accordance with recognized ethical guidelines. Studies were approved by an Institutional Review Board.

Real-Word Clinicogenomics Data

Clinicogenomics data from Tempus Labs Inc., coving all major cancer indications, were analyzed to explore overexpression and amplification prevalence across major tumor types. Tempus performed whole-exome RNA-seq, covering ~20,000 genes on clinical formalin-fixed, paraffin-embedded material from patients with cancer using a single platform. De-identified clinical and molecular data were analyzed from U.S. pan-cancer patient records. All statistical analyses were performed using R software version (4.2.1). To generate the pan-cancer HER2 overexpression threshold, a logistic regression model was fit to predict ERBB2 diploid or ERBB2 amplified (i.e., ≥6 copy number) status using HER2 expression. Using the computed threshold of 7.95 $\log_2$ [transcripts per million (TPM + 1)], prevalence of different ERBB2 alterations derived from DNA-seq (amplifications) and RNA-seq (gene expression) were plotted across tumor indications. On independent test data, the expression cutoff for HER2-high obtained a specificity and sensitivity of 0.92. For further details and data, see Supplementary Table S3.

In Vivo Experiments

For the cell line–based xenograft models, mice were group-housed (8–10 mice per cage) under pathogen-free and controlled environmental conditions (21°C ± 1.5°C temperature and 55% ± 10% humidity; 12-hour light–dark cycle) and handled according to the internal institutional, governmental, and European Union guidelines (Austrian Animal Protection Law, ETS-123). Animal studies were approved by the internal Ethics Committee and the local governmental committee. At 6 to 10 weeks old, female NMRI-*Foxn1*^{nu} mice (Taconic) were engrafted subcutaneously with 2.5 × 10^6 NCI-N87 cells, 5 × 10^6 PC-9 $EGFR^{KO}$,$HER2^{YVMA}$ cells, or 5 × 10^6 NCI-H2122 cells, respectively.

For PDX models, mice were group-housed under pathogen-free and controlled environmental conditions (20°C–23°C temperature and 30%–70% humidity) and handled according to institutional guidelines. Animal studies were approved by the Institutional Animal Care and Use Committees. At 6 to 8 weeks old, female athymic Nude-Foxn1nu (Envigo or Charles River Laboratories) were subcutaneously implanted with CTG-2534 or ST524 tumor fragments.

Tumor volumes were measured 2 to 3 times weekly using a caliper. Animals were weighed and examined daily and sacrificed based on severity criteria, including body weight, tumor size, and tumor necrosis. A maximum tumor size of 1,500 mm^3 was approved by the Ethics Committee for all models. Mice were sacrificed in case tumor volumes exceeded the limit between measurements. Data collection was performed blind to the condition of the experiments as compound codes were used. Data analysis was not performed blind to the condition of the experiment.

Activity Screen of Zongertinib across HER2 Mutations

This method was previously published (50) and adapted to HER2:

Cell Lines and Culture Conditions

Ba/F3 cells were maintained in RPMI1640 medium (Thermo Fisher Scientific) supplemented with 10% FBS, 2 mmol/L glutamine, 1% each of penicillin and streptomycin, and mouse IL3 (20 U/mL; Merck). The cells were used for the experiments within 10 passages from thawing. Cell line authentication and *Mycoplasma* testing were not carried out within 6 months.

MANO Method

A retroviral vector (pcx6-bleo) is utilized to enable stable integration of individual variants into the genome of the Ba/F3 cells along with the 10 bp barcode sequences upstream of the start codon of selected genes. Three clones with individual barcodes were constructed to obtain triplicate data for each assay (Azenta Life Sciences). The plasmids were transduced with packaging plasmids (Takara Bio) into HEK293T cells to produce recombinant retroviral particles. Ba/F3 cells were seeded on RetroNectin-coated (Takara Bio) plates and infected with retroviruses in a medium supplemented with 20 U/mL of IL-3. Ba/F3 cells expressing each variant were mixed in equal amounts and treated with the indicated concentrations of BI31 (100 pmol/L–10 μmol/L or 10% DMSO) as the vehicle control. The experiments were conducted in biological triplicate. At the end of the drug treatment, genomic DNA was extracted from the cell lysates using QIAmp DNA Mini Kit (Qiagen), and PCR amplification was performed using NEBNext Q5 Hor Start HiFi PCR Master Mix (New England Biolabs) according to the manufacturer's instructions and the primers shown in Supplementary Table S1. The amplicons were purified on AMPure beads (Beckman Coulter). Quality check of the libraries was assessed using a Qubit 2.0 fluorometer (Thermo Fisher Scientific) and the Agilent 2200 TapeStation System (Agilent). The libraries were then sequenced using an Illumina MiSeq system and Reagent Kit V2 (300 cycles), and 150 bp paired-end reads were created (the sequencing primer loaded into the MiSeq cartridge is described in Supplementary Table S1). The barcode sequences 5′-CTAGACTGCCNNNNNNNNNNGGATCACTCT-3′ (in which N denotes any nucleotide) were included in the sequencing results, and the number of each barcode in each mutant was quantified. The number of barcodes was used to calculate the cell viability of cells with the variants (Supplementary Table S1). Considering the different doubling times of the integrated cells, DMSO-treated cell mixtures were used as the reference control for normalizing each cell clone signal. The relative growth inhibition of each cell clone was calculated as 100 × (average read number across triplicates)/(average read number of the DMSO control). Variants with fewer than 100 barcode sequence reads were excluded from the analysis. The dose–response curves were fit to the observed cell viabilities using the drc package in R language. The two-parameter log-logistic function LL.2 was used with the following settings: upper (relative viability without drug) = 1, robust = "mean", and method = "Nelder-Mead". The IC_{50} value was defined as the inflection point on a dose–response curve.

Statistics and Reproducibility

For *in vivo* experiments, animals per group were determined using power analysis. Power analysis was performed for *in vivo* studies with a two-sided test, $\alpha = 0.05$ and power 0.80. Animals were randomized according to tumor size at 69 to 303 mm^3, tumor volume for cell line–derived models, or at 125 to 311 mm^3 tumor volume for CTG-2543 and 78 to 226 mm^3 for ST524 after fragment implantation ($n = 8$–10 per group). No datapoints were excluded from visualization and/or analysis.

PRISM Cell Line Viability Assay

PRISM is a high-throughput multiplexed cancer cell line viability screening platform developed by the Broad Institute of Massachusetts Institute of Technology and Harvard. Zongertinib and BI-1622 were tested in the PRISM assay on 931 cell lines at eight-point dose dilutions (3-fold step dilutions) with a treatment duration of 5 days. Note, that this collection of cell lines does not cover all HER2 oncogenic mechanisms (e.g., mutations). Zongertinib produced AUCs and quality-passing 844 cell lines (713 cell lines excluding hematopoietic and fibroblasts), whereas BI-1622 produced data for 882 cell lines (741 cell lines excluding hematopoietic and fibroblasts).

The minimum and maximum doses were set at 0.002286 and 5 μmol/L, respectively. HER2-high TPM values in analysis and visualizations were set to TPM 250 based on the logistic regression model in patient data to compute HER2 overexpression; this cutoff does not inform patient selection or stratification. Data processing from raw intensity values to computed AUC values for each dose–response curve is described in the Supplementary Methods. The analysis code is publicly available on the code repository GitHub (https://github.com/cmap/dockerized_mts). For further details and data, see Supplementary Table S2.

PRISM Methods

The current PRISM cell set consists of 931 cell lines representing more than 45 lineages, including both adherent and suspension/hematopoietic cell lines. These cell lines largely overlap with and reflect the diversity of the Cancer Cell Line Encyclopedia cell lines (see https://portals.broadinstitute.org/ccle). Cell lines were grown in RPMI 10% FBS without phenol red for adherent lines and RPMI 20% FBS without phenol red for suspension lines. Parental cell lines were stably infected with a unique 24-nucleotide DNA barcode via lentiviral transduction and blasticidin selection. After selection, barcoded cell lines were expanded and QCed (*Mycoplasma* contamination test, a single-nucleotide polymorphism test for confirming cell line identity, and barcode ID confirmation). Passing barcoded lines were then pooled (20–25 cell lines per pool) based on doubling time and frozen in assay-ready vials. Test compounds were added to 384-well plates and run at 8-point doses with 3-fold dilutions in triplicate. These assay ready plates were then seeded with the thawed cell line pools. Adherent cell pools were plated at 1,250 cells per well, whereas suspension and mixed adherent/suspension pools were plated at 2,000 cells per well. Treated cells were incubated for 5 days and then lysed. Lysate plates were collapsed together prior to barcode amplification and detection.

PRISM Barcode Amplification and Detection

Each cell line's unique barcode is located at the end of the blasticidin resistance gene and gets expressed as mRNA. These mRNAs were captured using magnetic particles that recognize polyA sequences. Captured mRNA was reverse-transcribed into cDNA, and then the sequence containing the unique PRISM barcode was amplified by PCR. Finally, Luminex beads that recognize the specific barcode sequences in the cell set were hybridized to the PCR products and detected using a Luminex scanner which reports signal as a median fluorescence intensity (MFI).

PRISM Data Processing

I. For each plate, we first normalized the logMFI ($\log_2$ MFI) of the DMSO wells to their median logMFI.

II. Each detection well contained 10 control barcodes in increasing abundances as spike-in controls. A monotonic smooth p-spline was fit for each control barcode detection well to normalize the abundance of each barcode to the corresponding value in the plate-wise median DMSO profiles. Next, all the logMFI values in the well were transformed through the inferred spline function to correct for amplification and detection artifacts.

III. Next, the separability between negative and positive control treatments was assessed. In particular, we used the error rate of the optimum simple threshold classifier between the control samples for each cell line and plate combination. Error rate is a measure of overlap of the two control sets and is defined as

$$Error = \frac{FP + FN}{n}$$

in which FP is false positive, FN is false negative, and n is the total number of controls. A threshold was set between the distributions of positive and negative control logMFI values (with everything below the threshold said to be positive and above said to be negative) such that this value is minimized. Additionally, we also filtered based on the dynamic range of each cell line. The dynamic range was defined as

$$DR = \mu^{-} - \mu^{+}$$

in which $\mu^{+/-}$ stood for the median of the normalized logMFI values in positive/negative control samples.

IV. We filtered out cell lines with error rates above 0.05 and a dynamic range less than 1.74 from the downstream analysis. Additionally, any cell line that had less than two passing replicates was also omitted for the sake of reproducibility. Finally, we computed viability by normalizing with respect to the median negative control for each plate. Log–fold change viabilities were computed as

$$\log viability = \log_2(x) - \log_2(\mu^{-})$$

in which $\log_2(x)$ is the corrected logMFI value in the treatment and $\log_2(\mu^{-})$ is the median corrected logMFI in the negative control wells in the same plate.

V. Log-viability scores were corrected for batch effects coming from pools and culture conditions using the ComBat algorithm, as previously described (68).

VI. We fit a robust four-parameter logistic curve to the response of each cell line to the compound:

$$f(x) = b + \frac{a - b}{1 + e^{s\log\frac{x}{EC50}}}$$

with the following restrictions:

1. We require that the upper asymptote of the curve be between 0.99 and 1.01
2. We require that the lower asymptote of the curve be between 0 and 1.01
3. We no longer enforce decreasing curves
4. We initialize the curve fitting algorithm to guess an upper asymptote of 1 and a lower asymptote of 0.5
5. When the standard curve fit fails, we now report the robust fits provided by the dr4pl R package

and compute AUC and IC_{50} values for each dose–response curve.

VII. Finally, the replicates were collapsed to a treatment-level profile by computing the median score for each cell line.

Data Availability

The data discussed in this publication have been deposited in NCBI's Gene Expression Omnibus and are accessible through Gene Expression Omnibus series accession number GSE252799 (https://www.ncbi.nlm.nih.gov/geo/query/acc.cgi?acc=GSE252799).

Authors' Disclosures

B. Wilding reports grants from the Austrian Promotion Agency during the conduct of the study; in addition, B. Wilding has a patent for WO2021/213800 pending and is a full-time employee of Boehringer Ingelheim. L. Woelflingseder reports grants from the Austrian Research Promotion Agency during the conduct of the study and personal fees from Boehringer Ingelheim RCV outside the submitted work and is a full-time employee of Boehringer Ingelheim RCV. A. Baum reports grants from the Austrian Research Promotion Agency FFG grants during the conduct of the study and personal fees from Boehringer Ingelheim RCV outside the submitted work and is a full-time employee of Boehringer Ingelheim RCV. K. Chylinski reports grants from the Austrian Research Promotion Agency during the conduct of the study and personal fees from Boehringer Ingelheim RCV outside the submitted work. G. Vainorius reports grants from the Austrian Research Promotion Agency during the conduct of the study and personal fees from Boehringer Ingelheim RCV outside the submitted work and is a full-time employee of Boehringer Ingelheim

RCV. N. Gibson reports other support from Boehringer Ingelheim & Co. KG outside the submitted work; in addition, N. Gibson has a patent for WO2024133325A1 pending. I.C. Waizenegger reports grants from the Austrian Research Promotion Agency during the conduct of the study and personal fees from Boehringer Ingelheim RCV GmbH & Co. KG outside the submitted work and is a full-time employee of Boehringer Ingelheim RCV GmbH & Co. KG. D. Gerlach reports grants from the Austrian Research Promotion Agency FFG during the conduct of the study and personal fees from Boehringer Ingelheim RCV outside the submitted work and is a full-time employee of Boehringer Ingelheim RCV. M. Augsten reports grants from the Austrian Research Promotion Agency during the conduct of the study and personal fees from Boehringer Ingelheim RCV GmbH Co. KG outside the submitted work and is a full-time employee of Boehringer Ingelheim RCV GmbH Co. KG. S. Tilandyova reports grants from the Austrian Research Promotion Agency during the conduct of the study and personal fees from Boehringer Ingelheim RCV outside the submitted work and is a full-time employee of Boehringer Ingelheim RCV. D. Scharn reports grants from the Austrian Research Promotion Agency during the conduct of the study; in addition, D. Scharn has a patent 20210332054 issued to Assignee: Boehringer Ingelheim International GmbH (Ingelheim am Rhein), a patent 20230374021 pending, and a patent 11608343 issued to Assignee: Boehringer Ingelheim International GmbH (Ingelheim am Rhein) and reports being a former employee of Boehringer Ingelheim. M.A. Pearson reports other support from Boehringer Ingelheim during the conduct of the study and outside the submitted work. J. Popow reports personal fees from Boehringer Ingelheim during the conduct of the study. A.C. Obenauf reports grants from Boehringer Ingelheim during the conduct of the study. N. Yamamoto reports grants from Boehringer Ingelheim during the conduct of the study and grants from Astellas, Chugai Pharmaceutical, Eisai, Taiho, Bristol Myers Squibb, Pfizer, Novartis, Eli Lilly, AbbVie, Daiichi Sankyo, Bayer, Boehringer Ingelheim, Kyowa Kirin, Takeda, Ono Pharmaceutical, Janssen Pharmaceuticals, MSD, Merck, GSK, Sumitomo Pharma, Chiome Bioscience, Otsuka, Carna Biosciences, Genmab, Shionogi, Toray, KAKEN, AstraZeneca, InventisBio, Rakuten Medical, Amgen, and Bicycle Therapeutics and personal fees from Eisai, Takeda, Boehringer Ingelheim, Cmic, personal fees from Chugai Pharmaceutical, Merck, Healios, Mitsubishi Tanabe, Rakuten Medical, Noile-Immune Biotech, and Daiichi Sankyo outside the submitted work. F.L. Opdam reports other support from Boehringer Ingelheim during the conduct of the study and is a principal investigator of studies with Astra zeneca, Boehringer Ingelheim, Crescendo, Cytovation, GSK, Incyte, Lilly, Merus, Pierre Fabre, Relay, RevMed, Roche, and Taiho, with institutional provision of intellectual property. S. Kohsaka reports grants from Boehringer Ingelheim during the conduct of the study and grants from Chordia Therapeutics, Eisai, Konica Minolta, CIMIC, and H.U. Group Research Institute. Group Research Institute outside the submitted work. N. Kraut reports grants from the Austrian Research Promotion Agency FFG during the conduct of the study and personal fees from Boehringer Ingelheim RCV outside the submitted work and is a full-time employee of Boehringer Ingelheim RCV. J.V. Heymach reports personal fees from AbbVie, AnHeart Therapeutics, BioCurity Pharmaceuticals, BioNTech, , DAVA Oncology, Eli Lilly, EMD Serono, Janssen Pharmaceuticals, , Moffitt Cancer Center, ModeX, Novartis Pharmaceuticals, OncoCyte, and Sanofi and personal fees and other support from Spectrum Pharmaceuticals, Takeda, Mirati Therapeutics, Bristol Myers Squibb, Boehringer Ingelheim, and AstraZeneca outside the submitted work. F. Solca reports grants from the Austrian Research Promotion Agency during the conduct of the study and personal fees from Boehringer Ingelheim RCV outside the submitted work and is a full-time employee of Boehringer Ingelheim RCV. R.A. Neumüller reports grants from the Austrian Research Promotion Agency (grant numbers 865390, 872827, and 879012) during the conduct of the study and personal fees from Boehringer Ingelheim RCV outside the submitted work; in addition, R.A. Neumüller has a patent for WO2021/213800 pending. No disclosures were reported by the other authors.

Authors' Contributions

B. Wilding: Conceptualization, data curation, supervision, visualization, writing–original draft, project administration, writing–review and editing. **L. Woelflingseder:** Data curation, supervision, writing–original draft. **A. Baum:** Formal analysis, investigation, writing–original draft. **K. Chylinski:** Formal analysis, supervision, writing–original draft. **G. Vainorius:** Formal analysis, investigation, methodology, writing–original draft. **N. Gibson:** Conceptualization, investigation, writing–original draft. **I.C. Waizenegger:** Data curation, supervision, writing–original draft. **D. Gerlach:** Software, formal analysis, visualization, writing–original draft. **M. Augsten:** Supervision, writing–original draft. **F. Spreitzer:** Investigation. **Y. Shirai:** Investigation. **M. Ikegami:** Investigation. **S. Tilandyova:** Investigation. **D. Scharn:** Data curation, supervision, investigation. **M.A. Pearson:** Writing–original draft. **J. Popow:** Data curation, writing–original draft. **A.C. Obenauf:** Supervision, writing–original draft. **N. Yamamoto:** Supervision, writing–original draft. **S. Kondo:** Supervision, writing–original draft. **F.L. Opdam:** Data curation, supervision, investigation. **A. Bruining:** Investigation. **S. Kohsaka:** Supervision, investigation. **N. Kraut:** Resources, supervision, writing–original draft, writing–review and editing. **J.V. Heymach:** Supervision, investigation. **F. Solca:** Supervision, writing–original draft, writing–review and editing. **R.A. Neumuller:** Conceptualization, supervision, investigation, visualization, writing–original draft, project administration, writing–review and editing.

Acknowledgments

We thank Michaela Mittermair, Ajna Logo, Jasmin Mucha, Regina Ruzicka, Robin Jacob, Alexandra Beran, Ida Dinold, Maria Rieger, Barbara Herzig, Richard Piribauer, Christian Salamon, Michaela Streicher, Katharina Mayr, Anton Stoiber, Alexandra Hörmann, Christoph Reiser, Sarah Oberndorfer, Ismet Srndic, Sabine Olt, and Eva Strauß for technical assistance. We thank Petr Knesl, Stefan Kornigg, Josef Balla, Jens Bruchhaus, Thomas Fett, Sophie Mitzner, Biljana Peric-Simov, Guido Scholz, Markus Spina, and Jasmin Zimmer for inhibitor synthesis. We thank Yunhai Cui and his team members for performing the MDCK *in vitro* assays. We thank project team members for their contributions, in particular, Valeria Santoro, Matthias Treu, Julian Fuchs, Heribert Arnhof, Dana Botesteanu, Paolo Chetta, Mark Petronczki, Dietrich Böse, Harald Engelhardt, Andreas Bergner, Stephan Zahn, and Peter Ettmayer. We thank Harald Weinstabl, Jens Quant, and Christian Haslinger for support of the program. Data upload to the Gene Expression Omnibus was completed by Małgorzata Kamuda. We thank Tempus AI for help in analyzing the real-world patient data, especially Emma Tung Corcoran, Stephanie LaHaye, and Martin Bontrager. PRISM data were generated in collaboration with the Broad Institute under the leadership of Matthew G. Rees, Melissa M. Ronan, and Jennifer A. Roth. Life Science Editors provided writing assistance. Research at Boehringer Ingelheim RCV was supported by the Austrian Research Promotion Agency (grant numbers: 865390, 872827, and 879012)

Note

Supplementary data for this article are available at Cancer Discovery Online (http://cancerdiscovery.aacrjournals.org/).

Received March 12, 2024; revised July 12, 2024; accepted September 4, 2024; published first September 5, 2024.

REFERENCES

1. Wang Z. ErbB receptors and cancer. Methods Mol Biol 2017;1652:3–35.
2. Hynes NE, MacDonald G. ErbB receptors and signaling pathways in cancer. Curr Opin Cell Biol 2009;21:177–84.
3. Citri A, Yarden Y. EGF–ERBB signalling: towards the systems level. Nat Rev Mol Cell Biol 2006;7:505–16.
4. Swain SM, Shastry M, Hamilton E. Targeting HER2-positive breast cancer: advances and future directions. Nat Rev Drug Discov 2023; 22:101–26.
5. Piccart-Gebhart MJ, Procter M, Leyland-Jones B, Goldhirsch A, Untch M, Smith I, et al. Trastuzumab after adjuvant chemotherapy in HER2-positive breast cancer. N Engl J Med 2005;353:1659–72.
6. Slamon DJ, Leyland-Jones B, Shak S, Fuchs H, Paton V, Bajamonde A, et al. Use of chemotherapy plus a monoclonal antibody against HER2 for metastatic breast cancer that overexpresses HER2. N Engl J Med 2001;344:783–92.
7. Verma S, Miles D, Gianni L, Krop IE, Welslau M, Baselga J, et al. Trastuzumab emtansine for HER2-positive advanced breast cancer. N Engl J Med 2012;367:1783–91.
8. Modi S, Saura C, Yamashita T, Park YH, Kim S-B, Tamura K, et al. Trastuzumab deruxtecan in previously treated HER2-positive breast cancer. N Engl J Med 2020;382:610–21.
9. Giordano SH, Franzoi MAB, Temin S, Anders CK, Chandarlapaty S, Crews JR, et al. Systemic therapy for advanced human epidermal growth factor receptor 2–positive breast cancer: ASCO guideline update. J Clin Oncol 2022;40:2612–35.
10. Connell CM, Doherty GJ. Activating HER2 mutations as emerging targets in multiple solid cancers. Esmo Open 2017;2:e000279.
11. Cocco E, Lopez S, Santin AD, Scaltriti M. Prevalence and role of HER2 mutations in cancer. Pharmacol Ther 2019;199:188–96.
12. Yan M, Parker BA, Schwab R, Kurzrock R. HER2 aberrations in cancer: implications for therapy. Cancer Treat Rev 2014;40:770–80.
13. Li BT, Lee A, O'Toole S, Cooper W, Yu B, Chaft JE, et al. HER2 insertion YVMA mutant lung cancer: long natural history and response to afatinib. Lung Cancer 2015;90:617–9.
14. Wang SE, Narasanna A, Perez-Torres M, Xiang B, Wu FY, Yang S, et al. HER2 kinase domain mutation results in constitutive phosphorylation and activation of HER2 and EGFR and resistance to EGFR tyrosine kinase inhibitors. Cancer Cell 2006;10:25–38.
15. Perera SA, Li D, Shimamura T, Raso MG, Ji H, Chen L, et al. HER2YVMA drives rapid development of adenosquamous lung tumors in mice that are sensitive to BIBW2992 and rapamycin combination therapy. Proc Natl Acad Sci U S A 2009;106:474–9.
16. Stephens P, Hunter C, Bignell G, Edkins S, Davies H, Teague J, et al. Lung cancer: intragenic ERBB2 kinase mutations in tumours. Nature 2004;431:525–6.
17. Yang S, Wang Y, Zhao C, Li X, Liu Q, Mao S, et al. Exon 20 YVMA insertion is associated with high incidence of brain metastasis and inferior outcome of chemotherapy in advanced non-small cell lung cancer patients with HER2 kinase domain mutations. Transl Lung Cancer Res 2021;10:753–65.
18. Riudavets M, Sullivan I, Abdayem P, Planchard D. Targeting HER2 in non-small-cell lung cancer (NSCLC): a glimpse of hope? An updated review on therapeutic strategies in NSCLC harbouring HER2 alterations. ESMO Open 2021;6:100260.
19. Suzawa K, Toyooka S, Sakaguchi M, Morita M, Yamamoto H, Tomida S, et al. Antitumor effect of afatinib, as a human epidermal growth factor receptor 2-targeted therapy, in lung cancers harboring HER2 oncogene alterations. Cancer Sci 2016;107:45–52.
20. Song Z, Lv D, Chen S, Huang J, Wang L, Xu S, et al. Efficacy and resistance of afatinib in Chinese non-small cell lung cancer patients with HER2 alterations: a multicenter retrospective study. Front Oncol 2021;11:657283.
21. Zhou N, Zhao J, Huang X, Shen H, Li W, Xu Z, et al. The efficacy of afatinib in patients with HER2 mutant non-small cell lung cancer: a meta-analysis. Transl Cancer Res 2020;9:3634–42.
22. Prelaj A, Bottiglieri A, Proto C, Lo Russo G, Signorelli D, Ferrara R, et al. Poziotinib for EGFR and HER2 exon 20 insertion mutation in advanced NSCLC: results from the expanded access program. Eur J Cancer 2021;149:235–48.
23. Elamin YY, Robichaux JP, Carter BW, Altan M, Gibbons DL, Fossella FV, et al. Poziotinib for patients with HER2 exon 20 mutant non–small-cell lung cancer: results from a phase II trial. J Clin Oncol 2022;40:702–9.
24. Le X, Cornelissen R, Garassino M, Clarke JM, Tchekmedyian N, Goldman JW, et al. Poziotinib in non-small-cell lung cancer harboring HER2 exon 20 insertion mutations after prior therapies: ZENITH20-2 trial. J Clin Oncol 2022;40:710–18.
25. Wang B-C, Kuang B-H, Liu X-X, Lin G-H. Poziotinib in non-small-cell lung cancer patients with HER2 exon 20 mutations: a pooled analysis of randomized clinical trials. Medicine (Baltimore) 2022;101: e31337.
26. Robichaux JP, Elamin YY, Tan Z, Carter BW, Zhang S, Liu S, et al. Mechanisms and clinical activity of an EGFR and HER2 exon 20–selective kinase inhibitor in non–small cell lung cancer. Nat Med 2018;24:638–46.
27. Hyman DM, Piha-Paul SA, Won H, Rodon J, Saura C, Shapiro GI, et al. HER kinase inhibition in patients with HER2- and HER3-mutant cancers. Nature 2018;554:189–94.
28. Zhou C, Li X, Wang Q, Gao G, Zhang Y, Chen J, et al. Pyrotinib in HER2-mutant advanced lung adenocarcinoma after platinum-based chemotherapy: a multicenter, open-label, single-arm, phase II study. J Clin Oncol 2020;38:2753–61.
29. Klufa J, Bauer T, Hanson B, Herbold C, Starkl P, Lichtenberger B, et al. Hair eruption initiates and commensal skin microbiota aggravate adverse events of anti-EGFR therapy. Sci Transl Med 2019;11:eaax2693.
30. Shi Y, Wang M. Afatinib as first-line treatment for advanced lung adenocarcinoma patients harboring HER2 mutation: a case report and review of the literature. Thorac Cancer 2018;9:1788–94.
31. Hoe HJ, Solomon BJ. Optimizing dosing of trastuzumab deruxtecan in HER2-mutant non–small-cell lung cancer: a reminder that more is not always better. J Clin Oncol 2023;41:4849–51.
32. Goto K, Goto Y, Kubo T, Ninomiya K, Kim S-W, Planchard D, et al. Trastuzumab deruxtecan in patients with HER2-mutant metastatic non–small-cell lung cancer: primary results from the randomized, phase II DESTINY-lung02 trial. J Clin Oncol 2023;41:4852–63.
33. Li BT, Smit EF, Goto Y, Nakagawa K, Udagawa H, Mazières J, et al. Trastuzumab deruxtecan in HER2-mutant non–small-cell lung cancer. N Engl J Med 2022;386:241–51.
34. Abuhelwa Z, Alloghbi A, Alqahtani A, Nagasaka M. Trastuzumab deruxtecan-induced interstitial lung disease/pneumonitis in ERBB2-positive advanced solid malignancies: a systematic review. Drugs 2022;82:979–87.
35. Nagasaka M, Ou S-HI. NRG1 and NRG2 fusion positive solid tumor malignancies: a paradigm of ligand-fusion oncogenesis. Trends Cancer 2022;8:242–58.
36. Laskin J, Liu SV, Tolba K, Heining C, Schlenk RF, Cheema P, et al. NRG1 fusion-driven tumors: biology, detection, and the therapeutic role of afatinib and other ErbB-targeting agents. Ann Oncol 2020;31:1693–703.
37. Hofmann MH, Gerlach D, Misale S, Petronczki M, Kraut N. Expanding the reach of precision oncology by drugging all KRAS mutants. Cancer Discov 2022;12:924–37.
38. Huang L, Guo Z, Wang F, Fu L. KRAS mutation: from undruggable to druggable in cancer. Signal Transduct Target Ther 2021;6:386.
39. Lopez-Chavez A, Carter CA, Giaccone G. The role of KRAS mutations in resistance to EGFR inhibition in the treatment of cancer. Curr Opin Investig Drugs 2009;10:1305–14.
40. Bekaii-Saab TS, Yaeger R, Spira AI, Pelster MS, Sabari JK, Hafez N, et al. Adagrasib in advanced solid tumors harboring a $KRAS^{G12C}$ mutation. J Clin Oncol 2023;41:4097–106.
41. de Langen AJ, Johnson ML, Mazieres J, Dingemans A-MC, Mountzios G, Pless M, et al. Sotorasib versus docetaxel for previously treated non-small-cell lung cancer with KRAS G12C mutation: a randomised, open-label, phase 3 trial. Lancet 2023;401:733–46.
42. Cassier PA, Dooms CA, Gazzah A, Felip E, Steeghs N, Rohrberg KS, et al. KontRASt-01 update: safety and efficacy of JDQ443 in KRAS G12C -mutated solid tumors including non-small cell lung cancer (NSCLC). J Clin Oncol 2023;41(Suppl 16):9007.

43. Sacher A, LoRusso P, Patel MR, Miller WH, Garralda E, Forster MD, et al. Single-agent divarasib (GDC-6036) in solid tumors with a KRAS G12C mutation. N Engl J Med 2023;389:710–21.
44. Awad MM, Liu S, Rybkin II, Arbour KC, Dilly J, Zhu VW, et al. Acquired resistance to $KRAS^{G12C}$ inhibition in cancer. N Engl J Med 2021;384:2382–93.
45. Ho CSL, Tüns AI, Schildhaus H-U, Wiesweg M, Grüner BM, Hegedus B, et al. HER2 mediates clinical resistance to the $KRAS^{G12C}$ inhibitor sotorasib, which is overcome by co-targeting SHP2. Eur J Cancer 2021;159:16–23.
46. Hong DS, Fakih MG, Strickler JH, Desai J, Durm GA, Shapiro GI, et al. $KRAS^{G12C}$ inhibition with sotorasib in advanced solid tumors. N Engl J Med 2020;383:1207–17.
47. Zhao Y, Murciano-Goroff YR, Xue JY, Ang A, Lucas J, Mai TT, et al. Diverse alterations associated with resistance to KRAS(G12C) inhibition. Nature 2021;599:679–83.
48. Skoulidis F, Li BT, Dy GK, Price TJ, Falchook GS, Wolf J, et al. Sotorasib for lung cancers with KRAS p.G12C mutation. N Engl J Med 2021;384:2371–81.
49. Wilding B, Scharn D, Böse D, Baum A, Santoro V, Chetta P, et al. Discovery of potent and selective HER2 inhibitors with efficacy against HER2 exon 20 insertion-driven tumors, which preserve wild-type EGFR signaling. Nat Cancer 2022;3:821–36.
50. Kohsaka S, Nagano M, Ueno T, Suehara Y, Hayashi T, Shimada N, et al. A method of high-throughput functional evaluation of EGFR gene variants of unknown significance in cancer. Sci Transl Med 2017;9:eaan6566.
51. Wagle M-C, Kirouac D, Klijn C, Liu B, Mahajan S, Junttila M, et al. A transcriptional MAPK pathway activity score (MPAS) is a clinically relevant biomarker in multiple cancer types. NPJ Precis Oncol 2018;2:7.
52. Yu C, Mannan AM, Yvone GM, Ross KN, Zhang Y-L, Marton MA, et al. High-throughput identification of genotype-specific cancer vulnerabilities in mixtures of barcoded tumor cell lines. Nat Biotechnol 2016;34:419–23.
53. Corsello SM, Nagari RT, Spangler RD, Rossen J, Kocak M, Bryan JG, et al. Discovering the anticancer potential of non-oncology drugs by systematic viability profiling. Nat Cancer 2020;1:235–48.
54. Cancer Genome Atlas Network. Comprehensive molecular portraits of human breast tumours. Nature 2012;490:61–70.
55. Cancer Genome Atlas Research Network; Kandoth C, Schultz N, Cherniack AD, Akbani R, Liu Y, et al. Integrated genomic characterization of endometrial carcinoma. Nature 2013;497:67–73.
56. Hoffmann T, Hörmann A, Corcokovic M, Zmajkovic J, Hinterndorfer M, Salkanovic J, et al. Precision RNAi using synthetic shRNAmir target sites. Elife 2023;12:RP84792.
57. Li BT, Michelini F, Misale S, Cocco E, Baldino L, Cai Y, et al. HER2-Mediated internalization of cytotoxic agents in ERBB2 amplified or mutant lung cancers. Cancer Discov 2020;10:674–87.
58. McFall T, Trogdon M, Guizar AC, Langenheim JF, Sisk-Hackworth L, Stites EC. Co-targeting KRAS G12C and EGFR reduces both mutant and wild-type RAS-GTP. NPJ Precis Oncol 2022;6:86.
59. Wu Y-L, Opdam F, Barve M, Tu H, Berz D, Rohrbacher M, et al. 34P Updated data from Beamion LUNG-1, a phase (ph) Ia/b trial of the HER2-specific tyrosine kinase inhibitor (TKI), zongertinib (BI 1810631), in patients (pts) with HER2 mutation-positive (m^+) NSCLC. ESMO Open 2024;9(Suppl 3):102613.
60. Wu Y-L, Johnson M, Soo R, Baktash N, Maier D, Eigenbrod-Giese S, et al. Abstract CT284: a phase 3 randomized controlled trial of zongertinib (BI 1810631) compared with standard of care in patients with locally advanced or metastatic nonsquamous non-small cell lung cancer harboring HER2 tyrosine kinase domain mutations: beamion LUNG-2. Cancer Res 2024;84(Suppl 7):CT284.
61. Behan FM, Iorio F, Picco G, Gonçalves E, Beaver CM, Migliardi G, et al. Prioritization of cancer therapeutic targets using CRISPR–Cas9 screens. Nature 2019;568:511–6.
62. McDonald ER 3rd, de Weck A, Schlabach MR, Billy E, Mavrakis KJ, Hoffman GR, et al. Project drive: a compendium of cancer dependencies and synthetic lethal relationships uncovered by large-scale, deep RNAi screening. Cell 2017;170:577–92.e10.
63. Mohr SE, Smith JA, Shamu CE, Neumüller RA, Perrimon N. RNAi screening comes of age: improved techniques and complementary approaches. Nat Rev Mol Cell Biol 2014;15:591–600.
64. Meyers RM, Bryan JG, McFarland JM, Weir BA, Sizemore AE, Xu H, et al. Computational correction of copy number effect improves specificity of CRISPR–Cas9 essentiality screens in cancer cells. Nat Genet 2017;49:1779–84.
65. Cui Y, Lotz R, Rapp H, Klinder K, Himstedt A, Sauer A. Muscle to brain partitioning as measure of transporter-mediated efflux at the rat blood–brain barrier and its implementation into compound optimization in drug discovery. Pharmaceutics 2019;11:595.
66. Sieger P, Cui Y, Scheuerer S. pH-dependent solubility and permeability profiles: a useful tool for prediction of oral bioavailability. Eur J Pharm Sci 2017;105:82–90.
67. Braun C, Sakamoto A, Fuchs H, Ishiguro N, Suzuki S, Cui Y, et al. Quantification of transporter and receptor proteins in dog brain capillaries and choroid plexus: relevance for the distribution in brain and CSF of selected BCRP and P-gp substrates. Mol Pharm 2017;14:3436–47.
68. Johnson WE, Li C, Rabinovic A. Adjusting batch effects in microarray expression data using empirical Bayes methods. Biostatistics 2007;8:118–27.